creative commons
COMMONS DEED

저작자표시-비영리-변경금지 2.0 대한민국

이용자는 아래의 조건을 따르는 경우에 한하여 자유롭게

- 이 저작물을 복제, 배포, 전송, 전시, 공연 및 방송할 수 있습니다.

다음과 같은 조건을 따라야 합니다:

저작자표시. 귀하는 원저작자를 표시하여야 합니다.

비영리. 귀하는 이 저작물을 영리 목적으로 이용할 수 없습니다.

변경금지. 귀하는 이 저작물을 개작, 변형 또는 가공할 수 없습니다.

- 귀하는, 이 저작물의 재이용이나 배포의 경우, 이 저작물에 적용된 이용허락조건을 명확하게 나타내어야 합니다.
- 저작권자로부터 별도의 허가를 받으면 이러한 조건들은 적용되지 않습니다.

저작권법에 따른 이용자의 권리는 위의 내용에 의하여 영향을 받지 않습니다.

이것은 이용허락규약(Legal Code)을 이해하기 쉽게 요약한 것입니다.

Disclaimer

dCollection

공학석사 학위논문

Integration of Population Balance Model with Computational Fluid Dynamics for Estimation of Oxygen Mass Transfer Rate in Bioreactor

2021년 8월

서울대학교 대학원

화학생물공학부

박 영 석

Integration of Population Balance Model with Computational Fluid Dynamics for Estimation of Oxygen Mass Transfer Rate in Bioreactor

지도교수 이 종 민

이 논문을 공학석사 학위논문으로 제출함

2021년 6월

서울대학교 대학원

화학생물공학부

박 영 석

박 영 석의 공학석사 학위논문을 인준함

2021년 6월

위 원 장 이 원 보

부위원장 이 종 민

위 원 남 재 욱

Abstract

Integration of Population Balance Model with Computational Fluid Dynamics for Estimation of Oxygen Mass Transfer Rate in Bioreactor

YoungSeok Bak

School of Chemical & Biological Engineering

The Graduate School

Seoul National University

This thesis presents a reliable integrated model of Computational Fluid Dynamics (CFD) and Population Balance Model (PBM) for the gas-liquid stirred tank for predicting oxygen mass transfer rates. Three constructed meshes were compared: unstructured, structured with thickness resolved, and zero-thickness structured mesh. The structured with thickness resolved meshes were selected as the best mesh. Then, the adjustable parameters in PBM kernels were estimated. The grid search method was employed, due to the strong non-linearity of the CFD-PBM model, based on the Bayesian optimization (BO) to improve the efficiency of searching. The final model was validated with experimental measurement results, and the validated model and the uniform bubble size model were compared. The

results show that the PBM model reflects the heterogeneity of the system better, therefore better predicting the occurrence of dead zones in the stirred tank. Finally, a case study was conducted to examine changes in oxygen mass transfer according to changes in viscosity. As the viscosity was increased to 10 times that of water, the volume-averaged oxygen mass transfer rate decreased by 28% as the viscosity increased 10 times, and an increase in the mixing rate of 5% and the aeration rate of 10% was estimated to recover 67% and 45% of reduced mass transfer rate, respectively.

Keyword: Computational Fluid Dynamics, Multiphase, Population Balance Model, Oxygen Mass Transfer, Bioreactor, Viscosity

Student Number: 2019-29645

Contents

Contents 3

List of Figures 4

List of Tables 5

1. Introduction 6

2. Modeling Approach 10

2.1 CFD Modeling of Gas-Liquid Multiphase Flow 10

2.2 Turbulence Modeling 15

2.3 Population Balance Modeling 16

2.3.1 Formulation of Method of Moments (MOM) 18

2.3.2 Formulation of QMOM 20

2.3.3 Kernels for Bubble Dynamics 23

2.4 Modeling of the Volumetric Mass Transfer Rate $kL\alpha$ 31

2.5 Parameter Estimation with Bayesian Optimization (BO) 33

3. Geometry, Grid, and Numerical Strategy 36

4. Simulation Results and Discussion 49

4.1 Sensitivity Test 49

4.2 Parameter Estimation 53

4.3 Model Validation 58

4.4 Comparison between Uniform Size Model and PBM Model 64

4.5 Oxygen Mass Transfer Rate Results in Viscosity Changes 67

5. Conclusion 71

References 72

Abstract in Korean (국문 초록) 76

List of Figures

Figure 1 Drag factor plot of Gimbun [2], based on the correlation of Behzadi [28] 13
Figure 2 Drag factor plot with switch function applied. 14
Figure 3 Tetrahedral volume elements (Left), ... 40
Figure 4 Side view of the ring sparger reactor. 41
Figure 5 Top view of the ring sparger reactor 42
Figure 6 Grid of unstructured mesh, side view (polyhedral, 288k) 43
Figure 7 Grid of unstructured mesh, rotor and top view (polyhedral, 288k) 44
Figure 8 Grid of structured mesh, side view (hexagonal, 666k) 45
Figure 9 Grid of structured mesh, rotor and top view (hexagonal, 666k) 46
Figure 10 Grid of structured mesh, zero-thickness, side view (hexagonal, 670k) 47
Figure 11 Grid of structured mesh, zero-thickness, rotor and top view (hexagonal, 670k) 48
Figure 12 Contours of gas volume fraction around the impeller (Left: zero-thickness, Right: 4mm-thickness) 50
Figure 13 Contours of gas volume fraction (Left: side view, Right: impeller view) 52
Figure 14 BO progress 1 54
Figure 15 BO progress 2 55
Figure 16 BO progress 3 56
Figure 17 Changes in local d32 during BO process 57
Figure 18 Comparison of local bubble sauter mean (d32) with previous works and this work(CFD-PBM) 60
Figure 19 Contour of Bubble size (Left: side view, Right: Impeller view) 61
Figure 20 Contour of gas volume fraction (Left: side view, Right: Impeller view) 62
Figure 21 Comparison of evaluated DOs. 63
Figure 22 Comparison of region-averaged d32 and KLa results 66
Figure 24 Change in volume-averaged mass transfer rate according to viscosity. 69
Figure 25 Change in dead-zone occurrence according to viscosity. 70

List of Tables

Table 1 Inlet boundary moments 39
Table 2 Results of mesh sensitivitiy test 51

1. Introduction

Since the development of the fermentation tank of penicillin in the 1940s [1], the biotechnology sector has grown up like a billion-dollar industry. Stirred tank multiphase reactor is widely used for biotherapeutic products. In order to gain the advantage of economy of scale, scale-up must be achieved while maintaining productivity. This requires design consideration to ensure that the material delivered to the cell is always at an appropriate level, even if scale-up is achieved. Therefore, an appropriate understanding of interphase transport phenomena is required. Nevertheless, due to insufficient understanding of hydrodynamics, the scale-up of bioreactor is still a challenging task [2].

The oxygen mass transfer rate is one of the most important materials delivered to the cell in the bioreactor. Sufficient oxygen supply is needed for cellular respiration, otherwise causes severe degradation of productivity [3]. Therefore, minimizing the insufficient oxygen supply area, called the 'dead zone', is a primary object in bioreactor design and control. Reliable models, which are able to take account of oxygen mass transfer rate, are needed for scale-up, design, and control of the bioreactor.

The oxygen mass transfer rate heavily depends on the hydrodynamics. The volumetric mass transfer rate ($k_L a$) is estimated by multiplication of interfacial area and mass transfer coefficient (K_L). If the hydrodynamics of the system is accurately known, one can calculate interfacial areas explicitly from it. However, the mass transfer coefficient can only be estimated. There exist some empirical correlations [2-6], but they are only capable of calculating the total volume average $K_L a$ value of the reactor. They have obvious limitations since the hydrodynamics of the reactor are often highly inhomogeneous. Therefore, in order to predict and respond to the occurrence of dead zones, it is necessary to be able to simulate the inhomogeneous hydrodynamics of the reactor accurately.

Computational fluid dynamics (CFD) has found successful application on various chemical reactors with inhomogeneous hydrodynamics [4-6]. Bioreactors are generally gas-liquid 2-phase systems where the liquid is a continuous phase and the gas is dispersed phase. Those multiphase simulations are generally realized via an Eulerian-Eulerian two-fluid model due to its suitable prediction performance, with relatively small computational cost than other alternatives. In the 2-phase CFD model, several governing equations like phase continuities, momentum equations are solved simultaneously. The phase interaction forces are added in the governing equations of each phase as a source term. Several forces, like a drag, lift virtual mass, should be considered between the gas and liquid phase, and it is well-known that the effect of the drag force is the most dominant [7]. As a result, many drag models are suggested and validated with experimental data. For dispersed gas bubbles within the liquid, Schiller-Naumann, Ishii-Zuber, and grace models are widely used [2, 8] [9].

Based on validated drag laws, early researches on the gas-liquid mixing tanks was performed with uniform bubble size assumption throughout the tank [10, 11]. Their models achieve fairly good agreement with experiment data, except around impeller discharge. The bubble size distribution is not uniform inside the stirred tank, as several experimental research showed [12, 13]. Since the bubble size directly determines drag forces which is the dominant interphase force, the effect of uniform bubble size assumption can be significant. Therefore, a model that does not consider the bubble size distribution may yield inaccurate predictions.

For the heterogeneous disperse phase system, the population balance model (PBM) is widely used as a framework to obtain the dynamics [14-16]. PBM represents systems of partial differential equation of number density distribution function (NDF), in which a function that represents the spatial distribution of any variable of the dispersed particle. (e.g. diameter) However, the full PDE requires a large amount

of computation and is difficult to converge. Therefore, many methodologies for simplification have been suggested, and each methodology has advantages and limitations [17]. Early studies for predicting the local bubble size in stirred tanks using a discretization based on the method of the class (MOC) [8, 18]. However, for accurate prediction of the evolution of the moments of the bubble size distribution, MOC requires more than 20 classes which means heavy computational costs. Alternatively, the QMOM [19] has been widely used in modeling gas-liquid stirred tanks recently [2, 9, 20], since it requires considerably less computational cost than the MOC while offering accurate prediction. In this work, the QMOM method was employed to solve bubble dynamics in a stirred tank.

In the preceding paragraphs, the research and methodologies for predicting accurate hydrodynamics of gas-liquid stirred tanks are described. Based on predicted hydrodynamics and local interfacial area, evaluation of local oxygen mass transfer has been performed. Laakkonen [8] suggested a model validated with the bubble size measurement data in 14 and 200L stirred tanks. Though, the model uses the MOC method to solve the PBM, which requires heavy calculation. Gimbun [2] proposed a model that fairly good agreement with experimental results. However, most of the prior studies have assumed that the viscosity of the liquid is the same as that of general water. Generally, it is known that the $k_L a$ values decrease with increasing liquid viscosity [21,22]. Empirical correlations suggest that $k_L a$ values are proportional to the order of -0.4 to -0.7 of liquid viscosity. According to the industry-scale fermentation bioreactor process data of Goldrick [23], the apparent viscosity of the reactor is the same as water, 1cp, at the beginning but increases up to 100cp at the end of the batch. From rigorous calculations using empirical correlations, it is concluded that $k_L a$ value can be reduced from 15% to 4% of the water-viscosity level. Thus, compared to the significant effect of viscosity increase on bioreactor's oxygen supply, there is a lack of case study for spatial changes.

In this research, a CFD-PBM model reflecting bubble size distribution was established, and the spatial variation of oxygen mass transfer rate due to changes in viscosity was analyzed. The QMOM method was implemented to solve the PBM and PBM kernels, proposed by Laakkonen, used to describe bubble's coalescence and breakage phenomena. Various structures of mesh were explored to accurately simulate a given geometry, and sensitivity tests were conducted to determine the final mesh structure and refinement. The model was validated with experimental data [8]. Based on the validated model, the spatial variation of $k_L a$ was analyzed as viscosities increase to 10cp under the same conditions.

2. Modeling Approach

2.1 CFD Modeling of Gas-Liquid Multiphase Flow

The Eulerian-Eulerian approach is employed for multiphase simulation in this work. In this approach, the continuous and disperse phases are assumed as interpenetrating media, having their local volume fractions with cumulative sum as one. The volume fractions are governed by the following continuity equations:

$$\frac{\partial(\alpha_k \rho_k)}{\partial t} + \nabla \cdot (\alpha_k \rho_k \boldsymbol{u}_k) = 0 \tag{1}$$

where $\alpha_l, \rho_l, \boldsymbol{u}_l$ are the volume, the density, and the velocity of the kth phase, respectively. Noted that the interphase mass transfer is negligible thus not included in Eq. (1). The momentum equation of the liquid phase is following:

$$\frac{\partial(\alpha_l \rho_l \boldsymbol{u}_l)}{\partial t} + \nabla \cdot (\alpha_l \rho_l \boldsymbol{u}_l \boldsymbol{u}_l) = -\alpha_l \nabla P + \nabla \cdot \tau_l + F_{lg} + \alpha_l \rho_l g \tag{2}$$

where τ_l is the stress-strain tensor of the liquid phase, g is the gravity acceleration, and F_{lg} is the interaction force between the gas and liquid phase, respectively. Forces acting between phases include drag force, virtual mass, lift force, etc. The effect of other than the drag force is secondary in gas-liquid stirred tanks [7]. Therefore, the effect of the virtual mass and lift force is not included in this work to reduce the computational cost, thus $\mathrm{F_{lg}}$ is simplified by a simple term for the drag force. The drag force term is following:

$$\mathrm{F_{lg}} = -\frac{3\rho_l \alpha_g \alpha_l \mathrm{C_D} |u_l - u_g| (u_l - u_g)}{4 d_{32}} \tag{3}$$

where $\mathrm{C_D}$ is a drag coefficient and $\mathrm{d_{32}}$ is the bubble Sauter mean diameter.

In CFD simulation, the drag model determines the drag coefficient. The effect of the drag model on the flow field is significant. Various drag models have been used for stirred tank reactors. Buffo [24] and Petitti [9] employed a drag model formulated in terms of the terminal velocity of a rising bubble in a stagnant liquid [25]. The drag coefficient equation is following:

$$\mathrm{C_D} = \frac{\frac{4}{3} d_b (\rho_l - \rho_d) g}{\rho_l U_T^2} \tag{4}$$

$$\mathrm{U_T} = \sqrt{\frac{2\sigma}{d_b \rho_l} + \frac{g d_b}{2}} \tag{5}$$

where $\mathrm{U_T}$ is the terminal velocity for isolated air bubbles in distilled water, and σ is surface tension, respectively. Those equations are known to apply in the typical bubble size range, from 2 to 10 mm, for a stirred tank. Yet, a quite rigorous assumption included, that all the bubbles are spherical thus have the same constant terminal velocity. Drag coefficient depends on the non-spherical shape of bubbles, and also on swarm [26]. The correlation of Ishii and Zuber (Eq. (4)) and Tomiyama [27] (Eq. (5)) for taking into account those effects are following:

$$\mathrm{C_D} = \max\left\{min\left(\frac{24}{Re}(1 + 0.15Re^{0.687}), \frac{72}{Re}\right), \frac{8}{3}\frac{Eo}{Eo + 4}\right\} \tag{4}$$

$$\mathrm{C_D} = \max\left\{\frac{24}{Re}(1 + 0.15Re^{0.687}), \min\left(\frac{8}{3}, \frac{2}{3}\sqrt{Eo}\right)\right\} \tag{5}$$

where Re and Eo are the bubble Reynolds number and Eotvos number which represents the ratio between gravitational to surface tension forces, respectively. The effect on drag for the ellipsoidal bubble regime is accounted for by the Eotvos number. Furthermore, the local bubble density also affects the drag coefficient. Behzadi [28] suggested a correlation for the drag coefficient of dense dispersion of bubbles:

$$C_{D,\text{dense}} = C_D \left(e^{3.64\alpha_g} + \alpha_g^{0.864}\right) \quad (6)$$

The formation of the bubble cavity behind the impeller blade also has to be considered. According to Lane [10] and Gimbun [2], it is possible to model the gas cavity by providing a certain modification to the drag coefficient. For the region of high gas volume fraction, the drag coefficient for an isolated bubble is used. Therefore, the cavity behind the blade is treated as an isolated bubble, rather than the dense bubble dispersion. Noted that using correlation of dense dispersion of bubbles for the cavity region resulting in the disappearance of the bubble cavity and over prediction of the gassed power number [2]. Gimbun employed the Ishii and Zuber drag model and the Gimbun's drag factor was employed with cavity modification for the void fraction higher than 70%. However, severe discontinuous points exist around 0.7 gas volume fraction (see Figure 1). In this work, in order to promote stability, a switch function is introduced in the range of gas volume fraction 0.6 to 0.8 to deal with discontinuity (see Figure 2). The drag model described above has been implemented via a FLUENT user-defined MACROS.

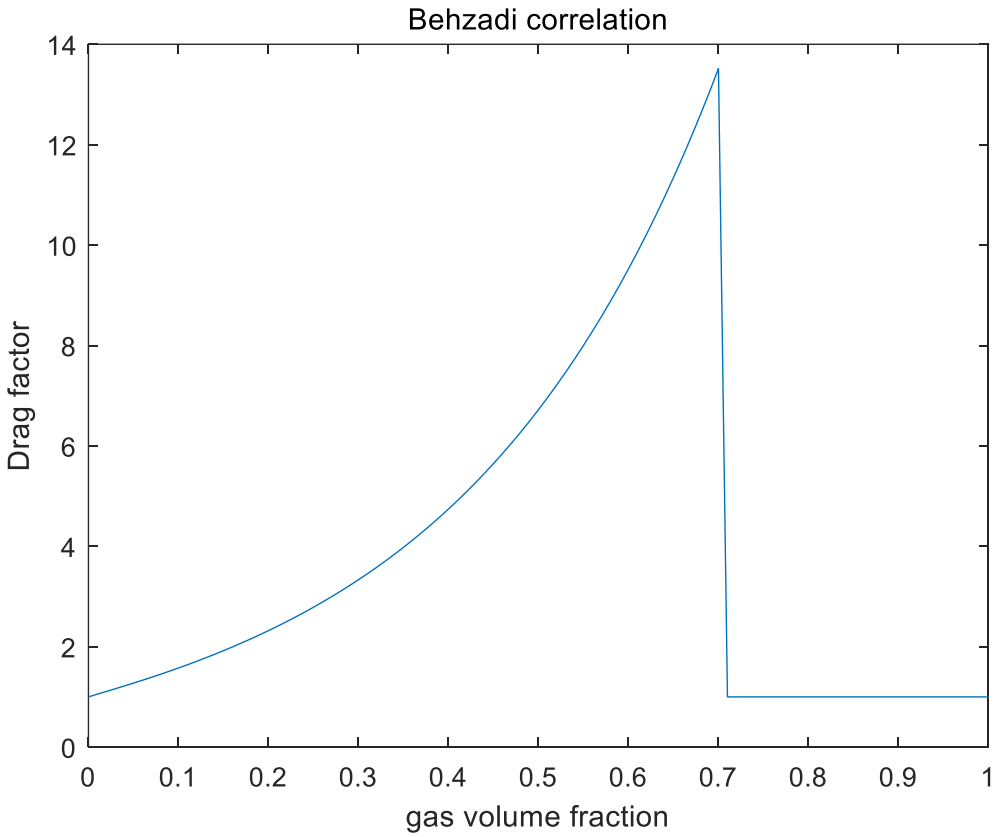

Figure 1 Drag factor plot of Gimbun [2], based on the correlation of Behzadi [28]

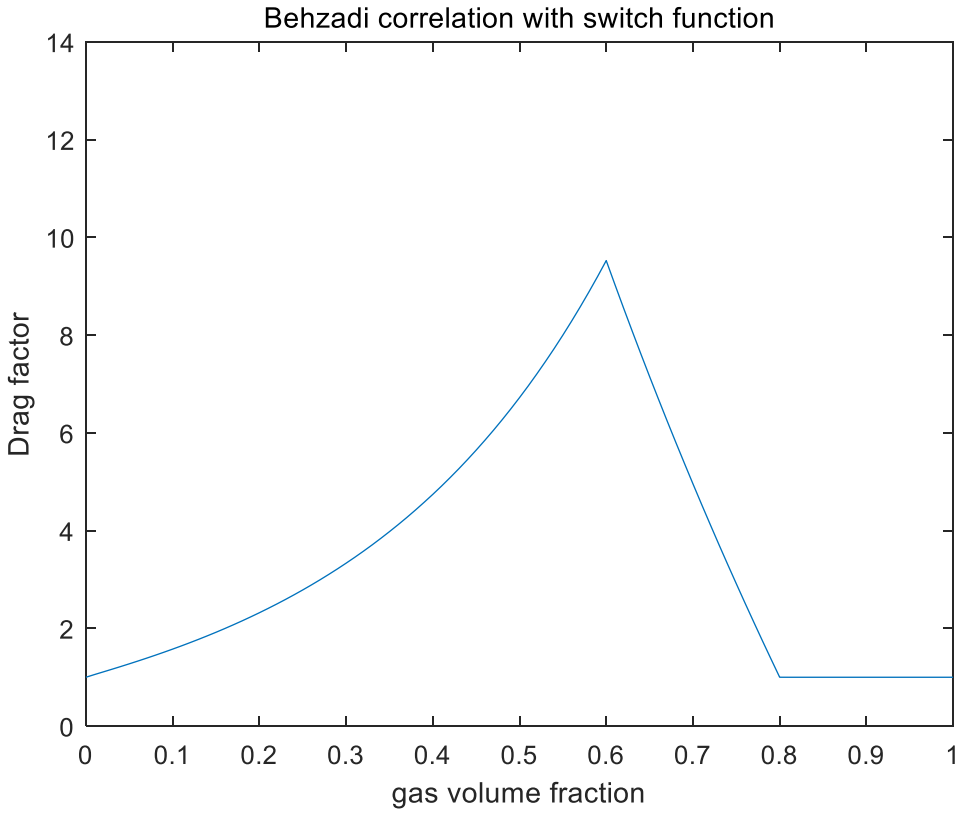

Figure 2 Drag factor plot with switch function applied.

(Switch function: $0.6 \leq gas\ volume\ fraction \leq 0.8$)

2.2 Turbulence Modeling

The Reynolds averaging Navier-Stokes (RANS) approach for turbulence is used. In Reynolds averaging, the flow variables in exact Navier-Stokes equations are decomposed into the ensemble-averaged and fluctuating components. As a result, The RANS equations are as following:

$$\frac{\partial \rho}{\partial t} + \frac{\partial}{\partial x_i}(\rho u_i) = 0 \tag{7}$$

$$\frac{\partial}{\partial t}(\rho u_i) + \frac{\partial}{\partial x_j}(\rho u_i u_j) = -\frac{\partial p}{\partial x_j}\left[\mu\left(\frac{\partial u_i}{\partial x_j} + \frac{\partial u_j}{\partial x_i} - \frac{2}{3}\delta_{ij}\frac{\partial u_l}{\partial x_l}\right)\right] + \frac{\partial}{\partial x_j}\left(-\rho\overline{u_i' u_j'}\right) \tag{8}$$

Additional terms, $-\rho\overline{u_i' u_j'}$, appear that represent the effects of turbulence, called Reynolds stresses, which must be modeled to close Eq. (9).

In this work, the SST $k-\omega$ mixture model was used for the modeling Reynolds stresses. The standard model parameter was used (i.e. $\sigma_{k,1} = 1.176, \sigma_{\omega,1} = 2.0, \sigma_{k,2} = 1.0, \sigma_{\omega,2} = 1.168, \alpha_1 = 0.31, \beta_{i,1} = 0.075, \beta_{i,2} = 0.0828$).

2.3 Population Balance Modeling

Due to bubble coalescence and breakage, the local values of bubble size and interfacial area can be changed. Since the interaction forces between phases directly depend on the interfacial area, those changes are an important aspect to be modeled. The population balance equation (PBE), in terms of a Number Density Function (NDF), is widely used to describe the bubble size evolution [29]. The number of particles has the value of internal coordinate (i.e. chemical composition, temperature, bubble size, etc.) within the range $(\mathrm{L}, \mathrm{L}+\mathrm{dL})$, and within the volume $\mathrm{d}\mathbf{x} = dx_1 dx_2 dx_3$ around the point $\mathbf{x} = (x_1, x_2, x_3)$ are expressed as:

$$\mathrm{n}(\mathrm{L}; \mathbf{x}, \mathrm{t})\mathrm{d}\mathbf{x}\mathrm{dL} \tag{9}$$

And the PBE can be expressed as:

$$\frac{\partial \mathrm{n}(\mathrm{L}; \mathbf{x}, \mathrm{t})}{\partial \mathrm{t}} + \nabla \cdot [\vec{u}\mathrm{n}(\mathrm{L}; \mathbf{x}, \mathrm{t})] = B_{ag}(\mathrm{L}; \mathbf{x}, \mathrm{t}) - D_{ag}(\mathrm{L}; \mathbf{x}, \mathrm{t}) + B_{br}(\mathrm{L}; \mathbf{x}, \mathrm{t}) - D_{br}(\mathrm{L}; \mathbf{x}, \mathrm{t}) \tag{10}$$

where $\mathrm{n}(\mathrm{L}; \mathbf{x}, \mathrm{t})$ is the NDF; L is the bubble size; x is the bubble velocity vector; $B_{ag}(\mathrm{L}; \mathbf{x}, \mathrm{t})$ and $D_{ag}(\mathrm{L}; \mathbf{x}, \mathrm{t})$ are the birth and death term arising from bubble coalescence; $B_{br}(\mathrm{L}; \mathbf{x}, \mathrm{t})$ and $D_{br}(\mathrm{L}; \mathbf{x}, \mathrm{t})$ are the birth and death terms due to bubble breakage, respectively. The change rate of bubble size mass transfer was neglected on the left side of Eq. (11).

Further assumptions for simplification are as follow [30]. In this work, the bubbles have the same chemical composition within the isothermal system. Moreover, the bubble velocity is assumed that linked to the bubble size with a known algebraic relationship. As a result, the bubble size only remains an internal coordinate. Then, the final PBE becomes:

$$\frac{\partial \mathrm{n_L}}{\partial \mathrm{t}} + \nabla \cdot [\vec{u}\mathrm{n_L}] = S_L \; = \; B_{ag,L} - D_{ag,L} + B_{br,L} - D_{br,L} \tag{11}$$

The source term in Eq. (12) consists of birth and death terms due to breakage and coalescence. A detailed description of those source terms are followed, first, the birth and death term due to coalescence can be calculated as [29]:

$$\mathrm{B_{ag,L}} = \frac{L^2}{2} \int_0^L \frac{K\left((L^3 + \lambda^3)^{\frac{1}{3}}, \lambda\right)}{(L^3 - \lambda^3)^{\frac{2}{3}}} n\left((L^3 + \lambda^3)^{\frac{1}{3}}\right) n(\lambda) d\lambda \tag{12}$$

$$\mathrm{D_{ag,L}} = \int_0^\infty K(L, \lambda) n(L) n(\lambda) d\lambda \tag{13}$$

where $\mathrm{K(L, \lambda)}$ is the coalescence kernel (coalescence frequency) related to two bubbles of size L and λ.

The birth and death term due to breakage are as follow:

$$\mathrm{B_{br,L}} = \int_L^\infty \beta(L, L') g(L') n(L') dL' \tag{14}$$

$$\mathrm{D_{br,L}} = \; g(L) n(L) \tag{15}$$

where g (L') is the Coalescence kernel of two bubbles with size L; and $\beta(\mathrm{L}, \lambda)$ is the daughter size distribution (DSD) distribution function for the formation of a daughter bubble L by the breakage of the mother bubble L'. The source term in moment space is unknown, therefore further modeling of the source term, called a kernel, is needed. It was covered in section 2.3.2.

2.3.1 Formulation of Method of Moments (MOM)

The above PBE (Eq. (12)) is a partial differential equation (PDE), which requires excessive computation and subroutines in the numerical process to be solved directly. Therefore, many simplification methods have been proposed, to practically solve PBE within the Eulerian-Eulerian framework. Early studies focused on the MOC method, which simplified PBE by discretizing the internal coordinate into appropriate intervals, and then integrating each interval. However, the MOC required dozens of bins, which required burdensome computations despite being simplified. Thus, the MOM was proposed by Randolph [31], which approximating the overall distribution of internal coordinates through moments. The advantage of the MOM is that its capability of reconstructing a relatively accurate distribution of internal coordinates, even with less than 6 moments. Hence, in order to predict the evolution of the moments of the bubble size distribution (BSD), the MOM is widely employed [31]. The moments of the bubble size distribution (BSD) with the above simplifications are defined as:

$$\mathrm{m_{L,k}} = \int_0^\infty n_{\mathrm{L}} \, L^k dL \;\; k = 0, 1, \cdots, 2N-1, \tag{16}$$

where k is the specified number of moments.

The PBE can be rewritten with this definition of moments:

$$\frac{\partial \mathrm{m_{L,k}}}{\partial t} + \nabla \cdot \left[\vec{u}\mathrm{m_{L,k}}\right] = \overline{\mathrm{S_{m_{L,k}}}} \tag{17}$$

$$\overline{\mathrm{S_{m_{L,k}}}} = \int_0^\infty S_L L^k \, dL \tag{18}$$

where $\overline{S_{m_{L,k}}}$ is the source term of moment space due to bubble coalescence and breakage. The limitation of early studies of MOM is the closure problem, where the source terms are not well defined in moments space. This was overcome by the introduction of QMOM [19], which will be explained in the next section.

2.3.2 Formulation of QMOM

As mentioned above, the QMOM has been overcome the closure problem of MOM [29, 32]. In QMOM, the sequence of polynomials orthogonal to the unknown NDF is determined from its moments. A Gaussian quadrature approximation is exploited. The source terms are estimated through the quadrature approximation. The roots of the polynomial of order N, orthogonal to the NDF, are the same as the nodes of the quadrature approximation. The approximation can be written as:

$$\int \mathrm{f}(\theta) n(\theta) d\theta \approx \sum_{i=1}^{N} f(\theta_i) w_i \tag{19}$$

where $\mathrm{f}(\theta)$ is the polynomial orthogonal to the NDF, $\mathrm{n}(\theta)$ is the unknown NDF, θ_i and $\mathrm{w_i}$ am i th node and weight of the quadrature approximation, and θ is an internal coordinate, respectively. If $\mathrm{f}(\theta)$ is a polynomial of order 2N -1 or smaller, this approximation (Eq. (20)) is exact [33].

By tracking the first 2N moments, a quadrature of order N can be constructed. However, while increasing the number of nodes in quadrature increases the accuracy, there is a trade-off that increases the computation cost and even makes the numerical problems. Therefore, in many gas-liquid systems such as bubble columns and stirred tanks, the use of three nodes with solving six-moment equations is widely employed as a choice that guarantees both accuracy and stability of CFD model [30, 32, 34]. Then the kth moment can be expressed as:

$$\mathrm{m_k} = \int_0^{\infty} n(L) L^k dL \approx \sum_{\mathrm{i=1}}^{\mathrm{N=3}} w_i L_i^k \tag{20}$$

An orthogonal polynomial family $\mathrm{P}_\alpha(L)$ are obtained using the recursive formula following [29]:

$$\mathrm{P}_{\alpha+1}(L) = (L - a_\alpha) P_\alpha(L) - b_\alpha P_{\alpha-1}(L);\ \alpha = 1 \cdots \mathrm{N}$$

(21)

$$a_\alpha = \frac{\int Ln(L)P_\alpha(L)P_\alpha(L)dL}{\int n(L)P_\alpha(L)P_\alpha(L)dL} \tag{22}$$

$$b_\alpha = \frac{\int n(L)P_\alpha(L)P_\alpha(L)dL}{\int n(L)P_{\alpha-1}(L)P_{\alpha-1}(L)dL} \tag{23}$$

The nodes of the quadrature approximation are the same as the zeros of $P_N(L)$. By similarity transformation, a matrix called the Jacobi matrix can be transformed from the systems of recursive equations above (Eq. (22)):

$$J = \begin{bmatrix} a_0 & \sqrt{b_1} & & & & \\ \sqrt{b_1} & a_1 & \sqrt{b_2} & & & \\ & \sqrt{b_2} & a_2 & \sqrt{b_3} & & \\ & & \ddots & \ddots & \ddots & \\ & & & \sqrt{b_{N-2}} & a_{N-2} & \sqrt{b_{N-1}} \\ & & & & \sqrt{b_N} & a_N \end{bmatrix} \tag{24}$$

The weights and nodes can be calculated from the above Jacobi matrix. Conversely, the Jacobi matrix can be calculated from moments efficiently by the Product-Difference algorithm [35] or Wheeler algorithm [36].

From the above QMOM formulation, the source term in Eq. (18) can be rewritten as:

$$\overline{S_{mk}} = \frac{1}{2}\sum_{i=1}^{N=3} w_i \sum_{j=1}^{N=3} w_j h_{ij}\left[\left(L_i^3 + L_j^3\right)^{\frac{k}{3}} - L_i^k - L_j^k\right] + \sum_{i=1}^{N=3} w_i g_i \left(\overline{b_i^k} - L_i^k\right) \tag{25}$$

where L_i and L_j are the nodes, w_i and w_j are the weights of the quadrature approximation; function h_{ij} and g_i are the coalescence kernel between bubbles of size L_i and L_j and the breakage kernel of bubbles size L_I; $\overline{b_i^k}$ is the kth moment of the daughter distribution function of daughter bubble size L, generated by the mother bubble size L_i, respectively. $\overline{b_i^k}$ can be calculated as follow:

$$\overline{b_i^k} = \int_0^{L_i} \beta(L, L_i) L^k dL \tag{26}$$

This explains most of the background theories of PBM modeling over QMOM. The next section covers the coalescence and break kernel and concludes the PBM part.

2.3.3 Kernels for Bubble Dynamics

Coalescence kernel

As a result of bubble collision, bubble coalescence may occur. Not only the interactions between bubbles but also interactions with continuous phases involve bubble coalescence. The coalescence kernel was introduced to describe such a phenomenon. The Coalescence kernel can be expressed as:

$$\mathrm{h}(L_1, L_2) = h_0(L_1, L_2)\lambda\,(L_1, L_2) \tag{27}$$

where $\mathrm{h}(L_1, L_2)$ is the coalescence kernel; $h_0(L_1, L_2)$ is the collision frequency and $\lambda\,(L_1, L_2)$ is the coalescence efficiency.

The collision frequency term describes the number of collisions per bubble per unit time and has units of m^3/s. The actual number of collisions between bubbles per unit time is expressed as a product of the number of particles per unit volume and the collision frequency. The collision efficiency term describes the fraction of collision events that result in coalescence and is a dimensionless number.

Coalescence frequency

Generally, the total collision frequency is considered as the sum of the contributions of several mechanisms (i.e. Turbulent fluctuations, buoyancy, wake-entrainment, etc.). Those mechanisms cause relative motion between bubbles. At medium superficial gas velocity, the turbulent fluctuations are the most important and the others are negligible [29]. In this work, only the contributions of turbulent fluctuation were considered. Thus, the collision frequency $h_0(L_1, L_2)$ is simplified to the turbulent collision frequency $h_0^T(L_1, L_2)$.

By analogy with the gas kinetic theory, Prince and Blanch calculated the bubble collision frequency due to turbulent eddies [37]. The turbulent collision frequency is calculated as follows

$$h_0^T(L_1, L_2) = \mathrm{S}_{12} u_{rel} \tag{28}$$

where S_{12} is the collision sectional area, u_{rel} is the relative approach velocity of two colliding bubbles.

The collision sectional area can be calculated as:

$$\mathrm{S}_{12} = \frac{\pi}{4}(L_1 + L_2)^2 \tag{29}$$

where L_1 and L_2 are the diameters of the colliding bubbles.

The most common assumption for calculating the relative velocity is that the colliding bubbles have the same velocity with an equal-sized eddy [38]. Therefore, the relative velocity is:

$$\mathrm{u}_{\mathrm{rel}} = \sqrt{2}\epsilon^{\frac{1}{3}}\sqrt{L_1^{2/3} + L_2^{2/3}} \tag{30}$$

The turbulent collision frequency can be rewritten as:

$$\mathrm{h}_0^T(L_1, L_2) = \sqrt{2}\frac{\pi}{4}(L_1 + L_2)^2\epsilon^{\frac{1}{3}}\sqrt{L_1^{2/3} + L_2^{2/3}} \tag{31}$$

Above expression modified by Prince and Blanch with an adjustable parameter C_1 [37]:

$$\mathrm{h}_0^T(L_1, L_2) = C_1(L_1 + L_2)^2\epsilon^{\frac{1}{3}}\sqrt{L_1^{2/3} + L_2^{2/3}} \tag{32}$$

Coalescence efficiency

Not every collision leads to coalescence events. There are three first-principle models representatively. the film-drainage model [39], the energy model [40], and the critical velocity models [41]. In this work, the coalescence efficiency based on the film-drainage model was used, and therefore, only the theory of the film-drainage models was covered. According to Coulaloglou, the coalescence efficiency can be expressed as [38]:

$$\lambda(\mathrm{L}_1, L_2) = \mathrm{e}^{-\frac{\mathrm{t_D}}{t_C}} \tag{33}$$

where $\mathrm{t_D}$ is the drainage time, and $\mathrm{t_C}$ is the contact time. Based on the film-drainage model, Coulaloglou and Tavlarides developed the following model for collision efficiency assuming that surface tension and inertial forces only control the drainage of an immobile bubble surface [38]:

$$\lambda(\mathrm{L}_1, L_2) = \exp\left(-C_2 \frac{\mu_l \rho_l \epsilon}{\sigma^2}\left(\frac{L_1 L_2}{L_1 + L_2}\right)^4\right) \tag{34}$$

where $\mathrm{C_2}$ is an adjustable parameter.

Finally, coupled with Eq. (19), (24), and (26), the total coalescence kernel can be rewritten:

$$\mathrm{h}(L_1, L_2) = C_1(L_1 + L_2)^2 \epsilon^{\frac{1}{3}} \sqrt{L_1^{2/3} + L_2^{2/3}} \exp\left(-C_2 \frac{\mu_l \rho_l \epsilon}{\sigma^2}\left(\frac{L_1 L_2}{L_1 + L_2}\right)^4\right) \tag{35}$$

Breakage kernel and daughter distribution function

A balance between external stresses caused by the continuous liquid phase, surface stresses of the bubble, and viscous stresses determines the bubble breakage phenomenon [42]. The main mechanisms involved can be divided into four groups: turbulent fluctuations and collisions, viscous shear forces, shearing-off process, interfacial instability. In the turbulent system, similarly to the coalescence phenomenon, the turbulent fluctuation is the most important.

The breakage resulting from turbulent fluctuation and collision can be classified into four cases: Case 1: the bubble has greater turbulence kinetic energy than a critical value; Case 2: the bubble surface is exposed to a velocity fluctuation larger than a critical value; Case 3: velocity fluctuation around the bubble surface greater than a critical value; Case 4: the inertial force of the hitting eddy

In order to describe breakage completely, not only the breakage frequency but also the number and the size of the generated bubbles are required to be considered. The daughter distribution function β includes that information. The daughter distribution functions are classified into three categories: empirical, statistical, phenomenological model.

Breakage kernel (frequency)

The research on breakage frequency has been studied in various multiphase systems. Coulaloglou and Tavlarides first proposed a breakage kernel for bubbles [38]. The theory of liquid-liquid dispersion was extended to bubbles. The breakage kernel of Coulaloglou and Tavlarides is following [38]:

$$\mathrm{g(L)} = c' L^{-\frac{2}{3}} \frac{\epsilon^{\frac{1}{3}}}{1+\alpha_g} \exp\left[-\frac{c''\sigma\left(1+\alpha_g\right)^2}{\rho_g \epsilon^{\frac{2}{3}} L^{\frac{5}{3}}}\right] \tag{36}$$

Prince and Blanch (1990) reported that the breakage kernel above generally results in an underpredicted breakage frequency. Therefore, the density of the gas is replaced by the density of liquid [43].

For drops in liquid, Alopaeus obtaining the following breakage kernel [44]:

$$g(L) = C_3 \epsilon^{\frac{1}{3}} \mathrm{erfc}\left(\sqrt{C_4 \frac{\sigma}{\rho_L \epsilon^{\frac{2}{3}} L^{\frac{5}{3}}} + C_5 \frac{\mu_g}{\sqrt{\rho_L \rho_G}\epsilon^{\frac{1}{3}} L^{\frac{4}{3}}}}\right) \tag{37}$$

From the similarity between mechanisms of bubbles and droplets, Laakkonen (2006) [45] modified the above kernel (Eq. 29) for a gas-liquid system.

$$g(L) = C_3 \epsilon^{\frac{1}{3}} \mathrm{erfc}\left(\sqrt{C_4 \frac{\sigma}{\rho_L \epsilon^{\frac{2}{3}} L^{\frac{5}{3}}} + C_5 \frac{\mu_l}{\sqrt{\rho_L \rho_G}\epsilon^{\frac{1}{3}} L^{\frac{4}{3}}}}\right) \tag{38}$$

The C_3 is a constant adjustable; the constants C_4 and C_5 are obtained by the turbulence theory, and have the magnitude of 0.04 and 0.01, respectively. In this work, the Laakkonen breakage kernel (Eq. 30) was employed to describe breakage frequency.

Daughter distribution function

Let the number of daughter bubbles produced as a result of breakage be N. The daughter distribution function must satisfy the following constraints:

$$\int_0^\infty \beta(L,\lambda)dL = N \tag{39}$$

$$\int_0^\infty \beta(L,\lambda)L^3dL = \lambda^3 \tag{40}$$

where L is the size of the daughter bubble and λ is the size of the mother bubble.

Based on β-distribution, the daughter distribution function of Laakkonen (2007) [8] is as follow:

$$\beta(L,\lambda) = \frac{1}{2}(1+C_6)(2+C_6)(3+C_6)(4+C_6)\left(\frac{L^2}{\lambda^3}\right)\left(\frac{L^3}{\lambda^3}\right)^2\left(1-\frac{L^3}{\lambda^3}\right)^{C_6} \tag{41}$$

Coupled with Eq. (31) and (33), a correlation between C_6 and N is:

$$N = \frac{4}{3}+\frac{C}{3} \tag{42}$$

Considering binary breakage, the value of C_6 is assumed to 2. Then, the daughter distribution function β can be rewritten as:

$$\beta(L,\lambda) = 180\left(\frac{L^2}{\lambda^3}\right)\left(\frac{L^3}{\lambda^3}\right)^2\left(1-\frac{L^3}{\lambda^3}\right)^2 \tag{43}$$

In this work, Eq. (44) was employed as a daughter distribution function. In FLUENT, the user can choose Eq. (35) as a built-in option. According to Laakkonen (2007), the best-fitted value of three adjustable parameters in Eq. (36) and (39) (C_1, C_2 and C_3) are 2.65, 5.17, and 2.52, respectively.

However, Laakkonen employed the MUSIG method, one of the MOC methods, was used for PBM solving, hence those parameter values are not adequate for this work. In this work, parameter exploration of C_1 and C_3 has been conducted. The results will be covered in Chap. 3.

2.4 Modeling of the Volumetric Mass Transfer Rate $k_L a$

For aerated stirred tanks bioreactor, many empirical correlations have been developed to calculate $k_L a$ [21, 46, 47]. Generally, obtaining equations such as the following [48]:

$$K_L a = C V_s^a \left(\frac{P}{V}\right)^b \mu_a^c \tag{44}$$

where C is a geometrical constant; P/V is the average power input per volume, V_s is the superficial gas velocity, μ_a is the liquid effective viscosity. The exponent values show a wide variation by different authors, for the liquid effective viscosity the range of exponent value is: $-0.4 \leq c \leq -0.7$.

However, correlations above are for the average $k_L a$ of the entire reactor, not for the local value. In order to maintain optimal productivity of a bioreactor, the occurrence of dead-zone, where the sub-minimum level of oxygen was transferred, should be well understood and managed, especially for larger-scale tanks.

For spherical bubble, the local interfacial area per unit volume can be calculated from Sauter mean as:

$$a = \sum_i \pi d_{b,i}^2 n_i \approx \frac{6 a_g}{d_{32}} \tag{45}$$

For ellipsoidal bubbles with diameters greater than around 3mm, the aspect ratio R from the correlation of Wellek [49]:

$$R = 1 + 0.163 E_o^{0.757} \tag{46}$$

where E_o is the Eotvos number. Though the above correlation was developed for liquid-liquid dispersion, Guet [50] reported that Eq. (47) is applicable for bubbles. In this work, for bubbles with

Sauter mean larger than 2mm, the local interfacial area was calculated using Eq. (46) and (47).

For calculating the volumetric mass transfer coefficient k_L, two models are widely used, the penetration model [51], and the eddy cell model [52]. The penetration model is based on Higbie's penetration theory, assuming that the contact time can be approximated as the Kolmogorov length scale. The penetration model varies slightly depending on the way the contact time is approximated. As one of the penetration models, the slip velocity model approximates contact time through slip velocity.

The slip velocity model results in k_L as:

$$k_L = \frac{2}{\sqrt{\pi}}\sqrt{\frac{D_L v_b}{d_b}} \tag{47}$$

where D_L is diffusivity and v_b is slip velocity

The eddy cell model results in k_L as:

$$k_L = K\sqrt{D_L\sqrt{\frac{\epsilon}{\nu}}} \tag{48}$$

where K is the constant with a value of 0.4, theoretically; D_L is diffusivity; and ν is kinematic viscosity, respectively. The diffusivity of oxygen in water is set as $1.92 \times 10^{-9}\, m^{-2}s$. According to Maltby [18] the slip velocity model provides the best fit to experimental $k_L a$ data. Therefore, in this work, the slip velocity model was employed to calculate the oxygen mass transfer rate.

2.5 Parameter Estimation with Bayesian Optimization (BO)

The CFD-PBM coupled model is highly non-linear because the hydrodynamics of CFD and the moments of PBM have a mutual effect. The coalescence and breakage kernels have a non-linear function form in many flow variables, adding unpredictability to the model. Parameter estimation of the above models with strong nonlinearity generally uses grid search-based methods, such as random search, since the gradient-based methodologies are not available. However, grid search is inefficient therefore inappropriate if the cost to obtain objective function values for the parameters is expensive such as CFD. Hence, the grid search should be carried out by constructing an efficient design of experiments by exploiting the prior knowledge of the model as much as possible. In this work, parameter estimation was conducted using BO for the efficient design of experiments [53].

BO is a type of nonlinear optimization that analyzes the stochastic surrogate model based on the iterative sampling of unknown objective functions [54]. The Gaussian process (GP) is the most accepted methodology for constructing the surrogate model. Concerning the N sample points and their objective function value $\mathrm{f}(\mathrm{x}_1) \ldots f(x_n)$, a Gaussian distribution whose mean and covariance matrix are expressed as:

$$\mathrm{f}_{1:\mathrm{N}} \sim N\left(m_{1:N}, K\right) \tag{49}$$

where the objective function value of the samples: $\mathrm{f}_{1:\mathrm{N}} = \left(f(x_1) \ldots f(x_n)\right)^T$; the mean function: $\mathrm{m}_{1:\mathrm{N}} = \left(m(x_1) \ldots m(x_n)\right)^T$; the covariance kernel function: $\mathrm{K}\left(\mathrm{x}_\mathrm{i}, x_j\right)$. The covariance kernel functions reflect a prior belief of the objective function. In this work, the Isotropic Matern 5/2 kernel applied:

$$\mathrm{k}(\mathrm{x}_i, x_j) = \sigma_f^2 \left(1 + \frac{\sqrt{10}r}{\rho} + \frac{10\mathrm{r}^2}{3\rho^2}\right) \exp\left(-\frac{\sqrt{10}r}{\rho}\right) \tag{50}$$

where σ_f and ρ are the hyper-parameters. Eq. (51) indicates the closer the distance between two sample points in the sample space is, the stronger the correlation is between their objective function values. The prediction of the unknown objective function value at point x' is conducted using the characteristic that $\mathrm{f}_{1:\mathrm{N}}$ and $\mathrm{f}_{\mathrm{x}'}$ have a joint Gaussian distribution also:

$$\begin{pmatrix} \mathrm{f}_{1:\mathrm{N}} \\ \mathrm{f}_{\mathrm{x}'} \end{pmatrix} \sim \mathcal{N}\left(\begin{pmatrix} \mathrm{m}_{1:\mathrm{N}} \\ \mathrm{m}_{\mathrm{x}'} \end{pmatrix}, \begin{pmatrix} \mathrm{K} & \mathrm{K}_{\mathrm{x}'} \\ \mathrm{K}_{\mathrm{x}'}^{\mathrm{T}} & \mathrm{K}_{\mathrm{x}'\mathrm{x}'} \end{pmatrix}\right) \tag{51}$$

where $\mathrm{f}_{\mathrm{x}'} = f\ (x')$; $\mathrm{m}_{\mathrm{x}'} = m(x')$; $\mathrm{K}_{\mathrm{x}'} \equiv \left(k(x_1, x') \ldots k(x_N, x')\right)^T$; and $\mathrm{K}_{\mathrm{x}'\mathrm{x}'} = k(x', x')$.

By receiving an objective function value at the newly added sampling point, the surrogate model is updated. The acquisition function provides a criterion to determine the next sampling point. The expected improvement (EI) is widely used as the acquisition function [55]. The definition of the improvement I is as follow:

$$\mathrm{I}(\mathrm{f}(\mathrm{x}')) \equiv \left(\min(f_{1:N}) - f(x')\right) \cdot 1_{[\min(f_{1:N}) > f(x')]} \tag{52}$$

where the indicator function, $1_{[\mathrm{E}]}$, has a value of 1 if E is true and 0 for else. The expectation of the improvement is as:

$$\begin{aligned} \mathrm{EI} \equiv\ & \mathrm{E}\left[\mathrm{I}(\mathrm{f}(\mathrm{x}'))\right] \\ &= (\min(f_{1:N}) - \mu')\Phi\left(\frac{\min(f_{1:N}) - \mu'}{\sigma'}\right) \\ &+ \sigma'\phi\left(\frac{\min\left(f_{1:N} - \mu'\right)}{\sigma'}\right. \end{aligned} \tag{53}$$

where $E[\cdot]$ is the expected value; $\Phi(\cdot)$ is the cumulative distribution function; $\phi(\cdot)$ is the probability density function of a normal distribution, respectively.

The BO process is implemented in MATLAB. The object function was chosen as square mean error from the local bubble size measurement at 390rpm, 0.7vvm, 200L stirred tank [8].

3. Geometry, Grid, and Numerical Strategy

In CFD models, the mesh has a significant impact on model results and convergence. In general, the number of elements in geometry and accuracy tends to trade-off. Therefore, in order to obtain accurate model results, the appropriate level of grid refinement is required so that the model reaches the grid-independent solution. In this work, a grid sensitivity test was performed using meshes with various structures and refinement to reach the grid-independent solution.

In 3D CFD modeling, the mesh structure used can be divided into two types: unstructured and structured. The unstructured mesh consists mainly of volume elements of tetrahedral or polyhedral, while the structured mesh consists of hexagonal volume elements strictly. Volume elements in each form are illustrated in Figure 3. The unstructured meshes are relatively easy to construct, but due to their inconsistent element shape, numerical instability can occur. On the other hand, the structured meshes promise relatively robust results due to their consistent element form, but they may require significant user effort to construct or even fail to generate depends on the geometry complexity. Generally, the structured meshes are preferred because they require relatively less computation to reach precise results.

Previous works have presented various criteria for mesh structure and refinement when CFD is used to simulate stirring tanks with blades and baffles. Derksen [56] concluded that at least eight grids must be used for impeller blade height to accurately resolve the vortex core structure by the blade. According to Gimbun, the model using 11 nodes for impeller blade height did not differ from the model using more nodes.

In order to resolve the thickness of blades and baffles, remarkable mesh refinement is required and

thus the computation cost increases significantly. As a kind of circumvent method, many studies have been conducted that assume the blades and baffles as zero thickness [57]. Coroneo showed good agreement with the results of the liquid-liquid dispersion experiment. However, the blade thickness is known to be a factor that influences the hydrodynamics of the system [58, 59]. Hence, Zadghaffari [60] pointed out that the zero-thickness assumption is not realistic.

In this work, a grid sensitivity test was conducted to find grids that guarantee accurate prediction and convergence stability. In order to compare structured mesh and unstructured mesh, both meshes were constructed and compared. And to test the zero-thickness assumption, the structured mesh was constructed and compared in geometry with thickness and zero-thickness. The comparison of structured and unstructured mesh was conducted with the geometry with thickness. In non-zero-thickness geometry, the thickness of blades and baffles is set to 4 mm, similar to the realistic value of the Rushton turbine [58]. The PBM is implemented using the built-in framework in FLUENT, however, the built-in kernels within the framework are limited, so the desired kernels were implemented using the USER DEFINE FUNCTION in FLUENT.

For CFD modeling, a 200L aerated stirred tank with 6-blades Rushton turbine, studied by Laakkonen [8], were considered. The turbine has a mixing rate of 390rpm and a gas was injected through a ring sparger at a flow rate of 0.7vvm, which is set to be the same as experimental conditions of Laakkonen. The interphase drag coefficient was estimated using the Ishii-Zuber model with the Behzadi correlation with switch function as drag factor. In order to model the impeller movement, a multiple reference frame was used. For turbulence and multiphase modeling, the Eulerian-Eulerian approach and SST $k-\omega$ model were employed. The coupled algorithm, with the pseudo-transient setting, was used. A Green-Gauss node-based formulation is considered for calculating gradients. QUICK scheme for the

momentum equation, PRESTO! Scheme for the pressure, and the 1st order upwind scheme for other equations were used. Rather than using a fictitious degassing outlet, a pressure outlet was used for the outlet boundary condition. For the inlet boundary condition, the gas is set to be released homogeneously in the sparger. The 12 holes in the actual sparger are omitted for geometry simplification. Inlet moments are also set to form boundary conditions in moments space. Moments were calculated to be the normal distribution with 19mm bubble size on average and 3.04mm deviation, according to observation data and the correlation of Gary and rice. Inlet boundary moments can be found in Table 1. Lastly, the overall gas holdup, inlet-outlet gas flow balances, and volume-average Sauter mean for the PBM model were used as convergence indicators.

A grid sensitivity study was performed using 7 different meshes: meshes with unstructured polyhedral volume elements (coarse: 288k, fine: 522k elements), meshes with structured hexagonal volume elements (419k, 666k, 729k, 930k elements), hexagonal structured mesh with zero-thickness blades and baffles (670k). It was found that the 666k non-zero-thickness structured mesh showed the best performance and was applied to simulations after. The grid features are summarized in the following figures. (Figure 6, Figure 7, Figure 8, Figure 9, Figure 10, Figure 11)

Table 1 Inlet boundary moments

Inlet boundary moments	
m0	258586.3
m1	4913.1
m2	93.3497
m3	1.7736
m4	0.0337
m5	6.40E-04

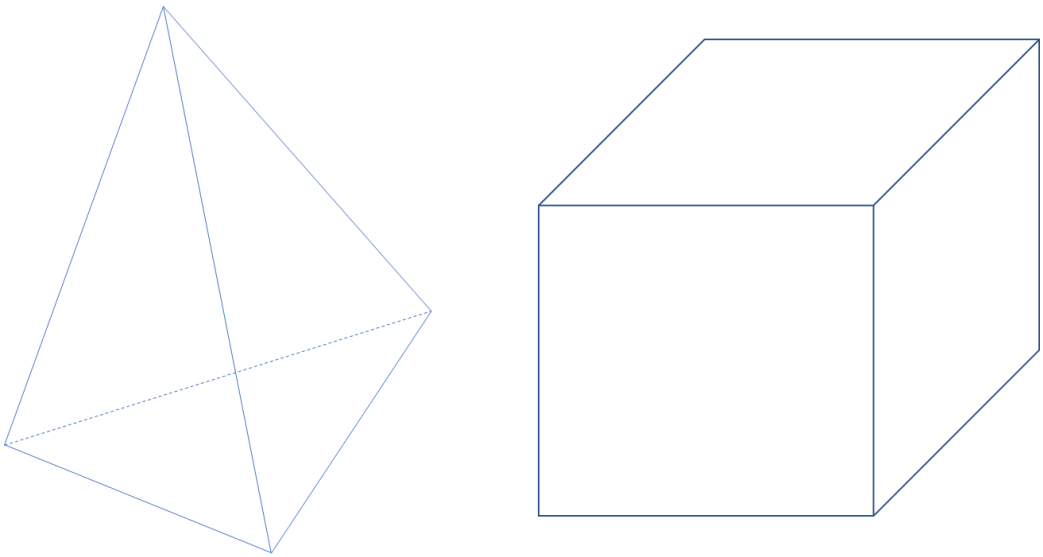

Figure 3 Tetrahedral volume elements (Left),

hexagonal volume elements (Right)

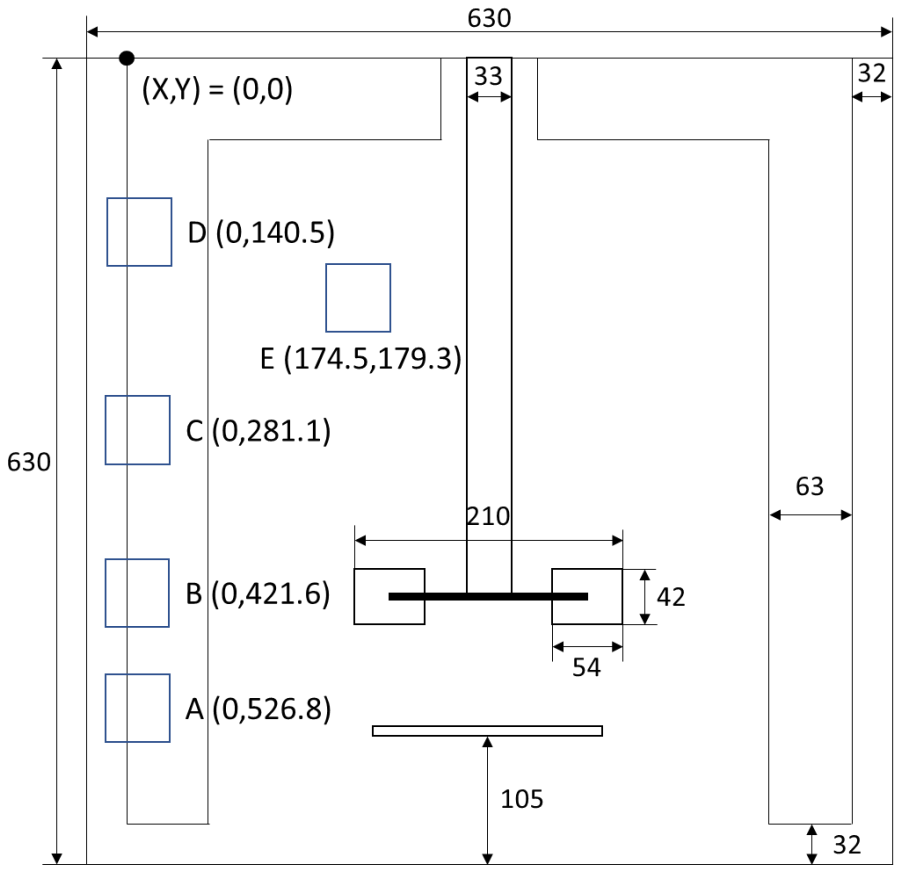

Figure 4 Side view of the ring sparger reactor.

(The axial points configuration, for which measurement data are available, are marked)

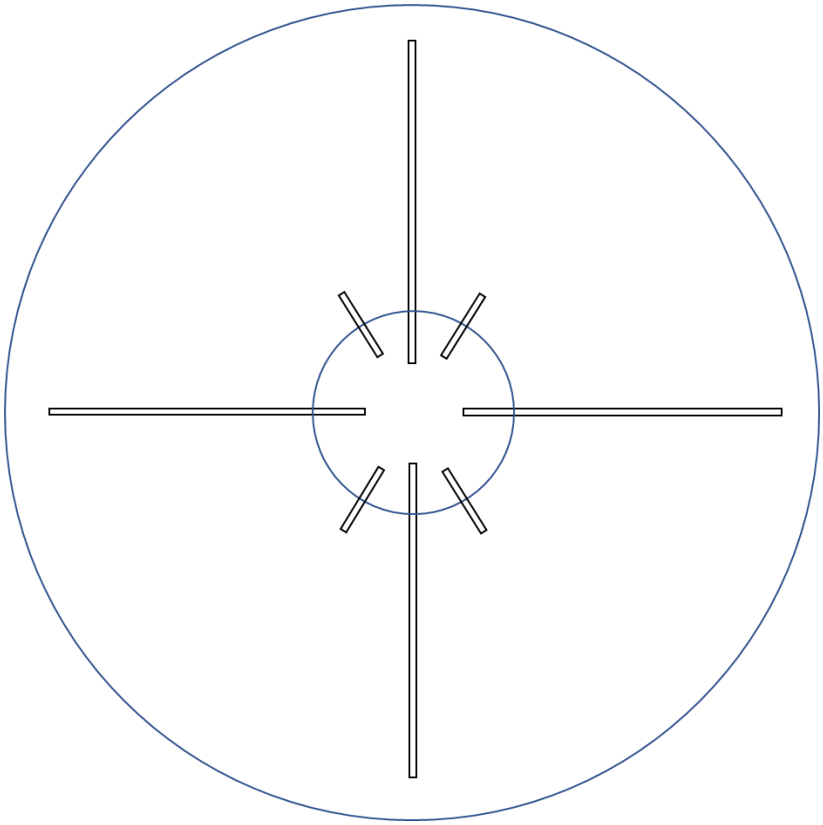

Figure 5 Top view of the ring sparger reactor

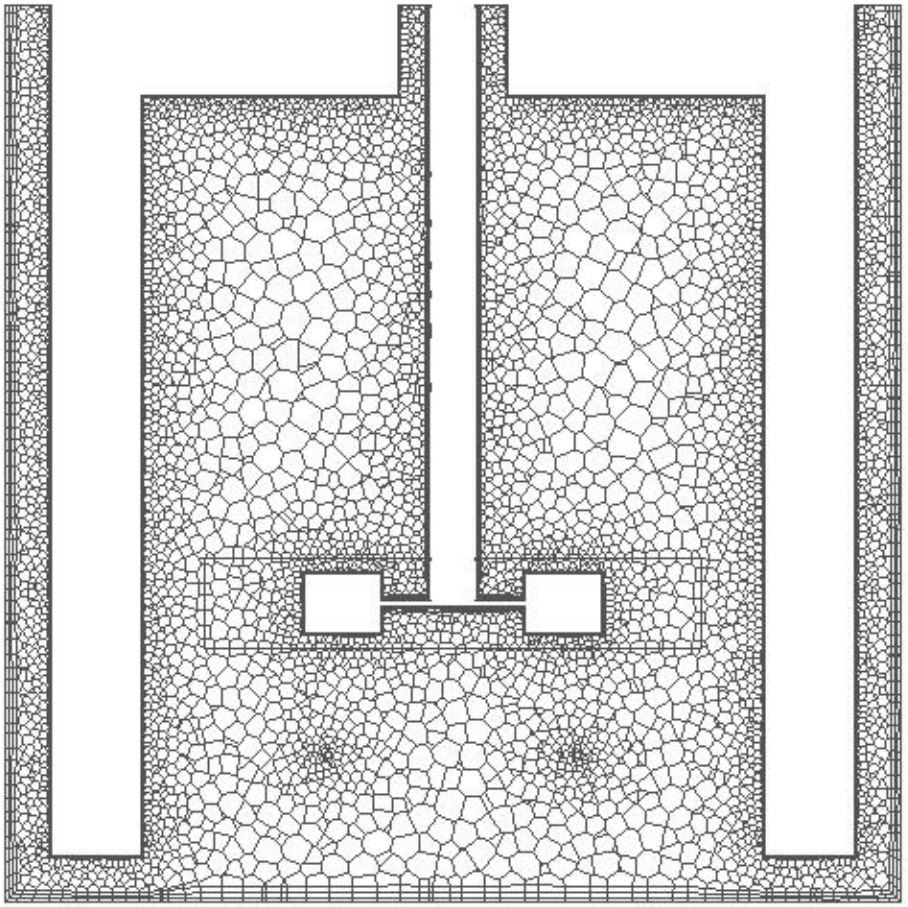

Figure 6 Grid of unstructured mesh, side view (polyhedral, 288k)

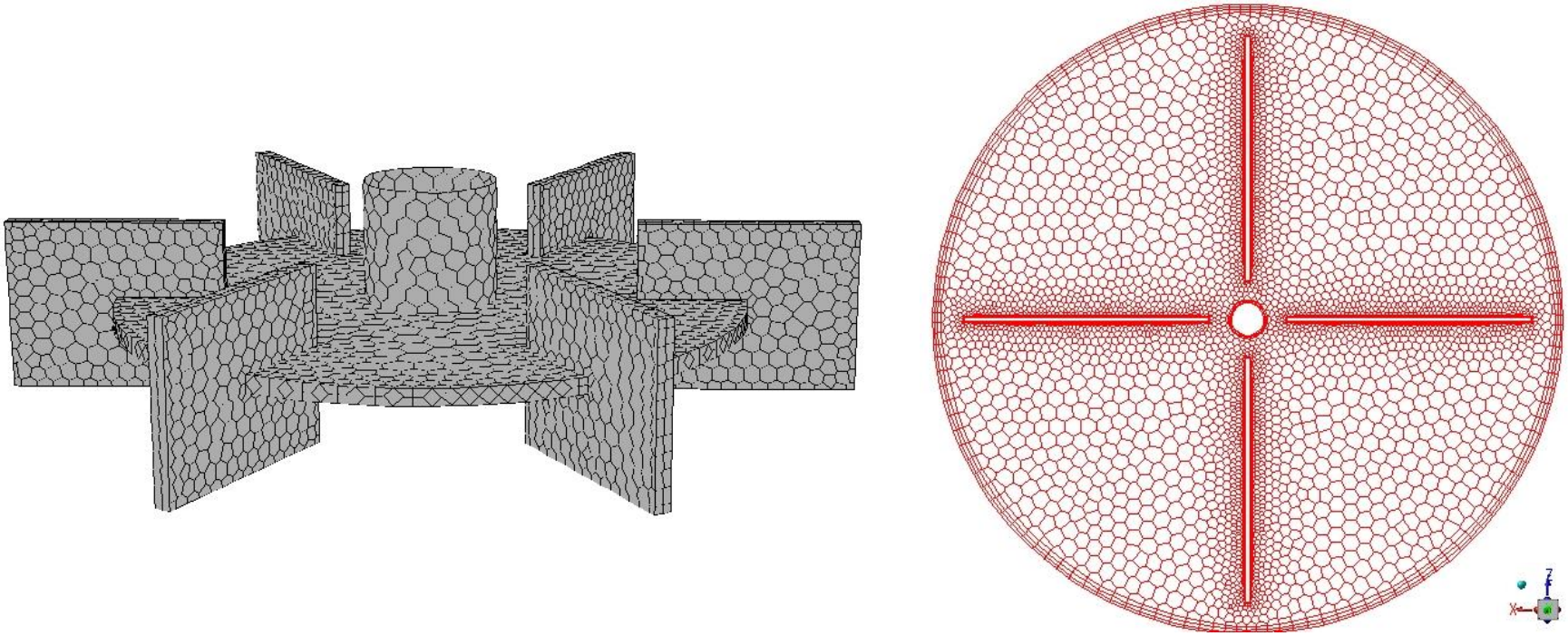

Figure 7 Grid of unstructured mesh, rotor and top view (polyhedral, 288k)

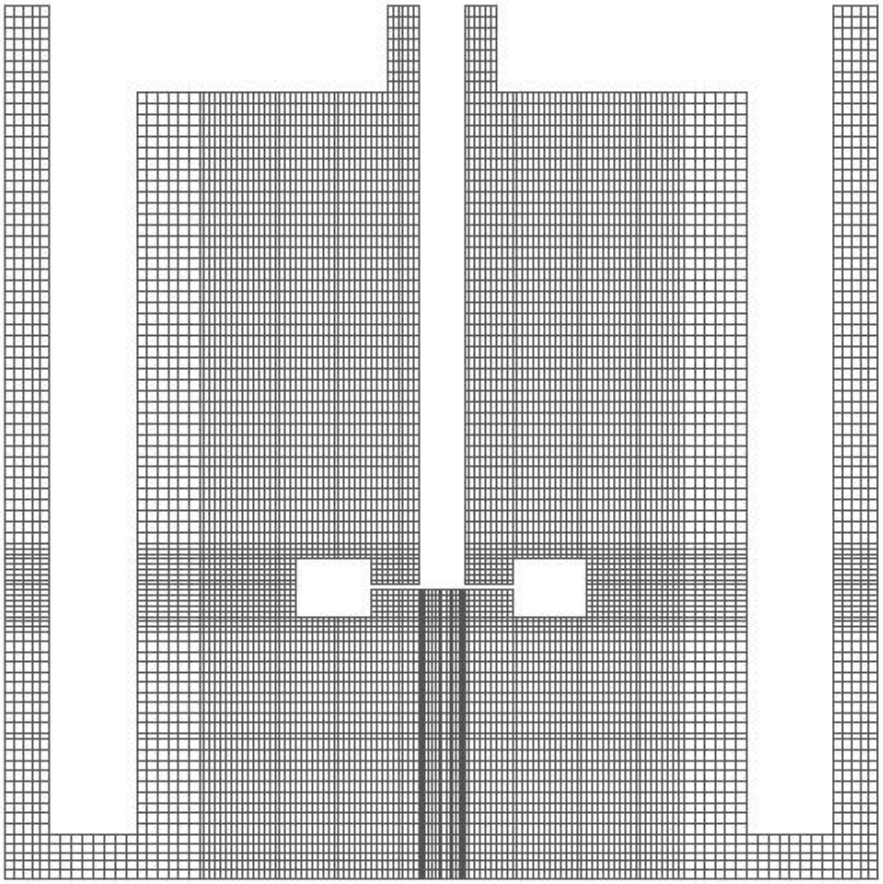

Figure 8 Grid of structured mesh, side view (hexagonal, 666k)

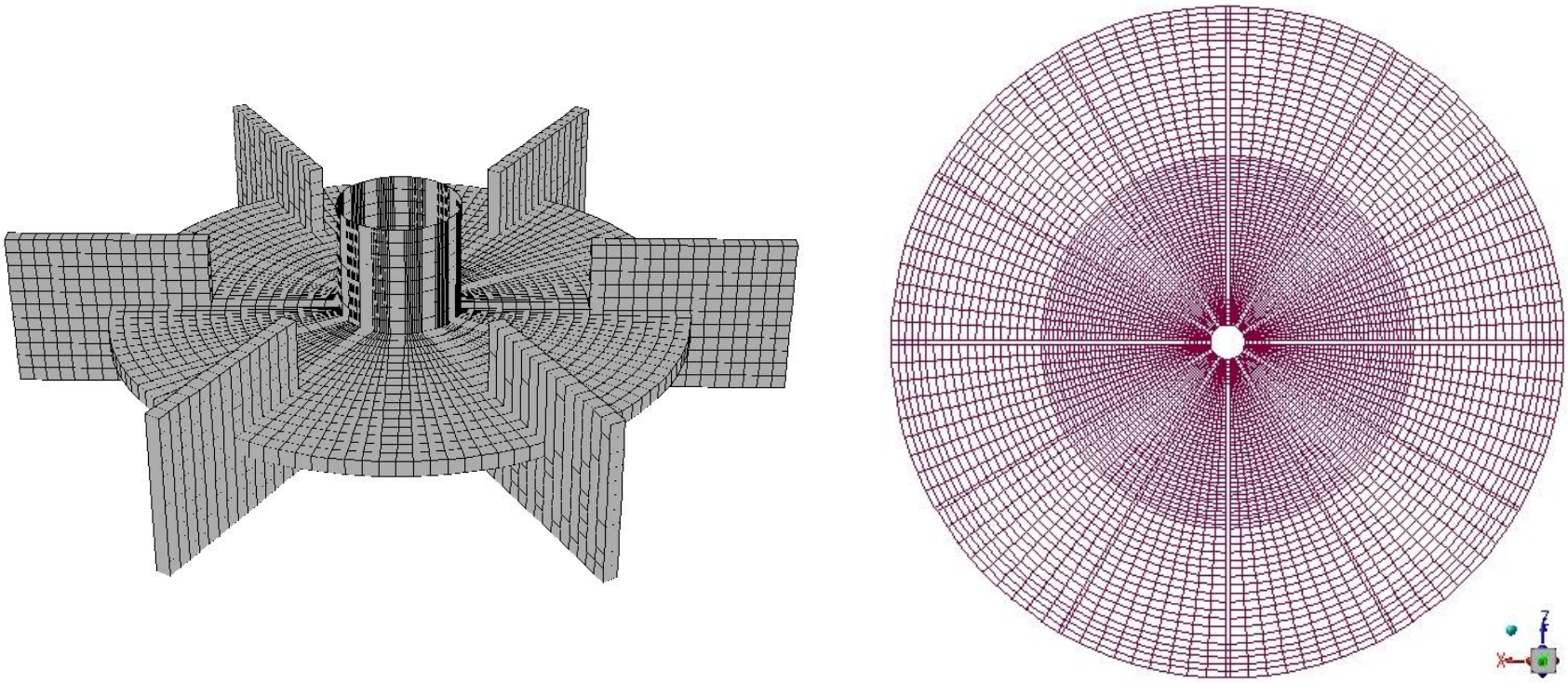

Figure 9 Grid of structured mesh, rotor and top view (hexagonal, 666k)

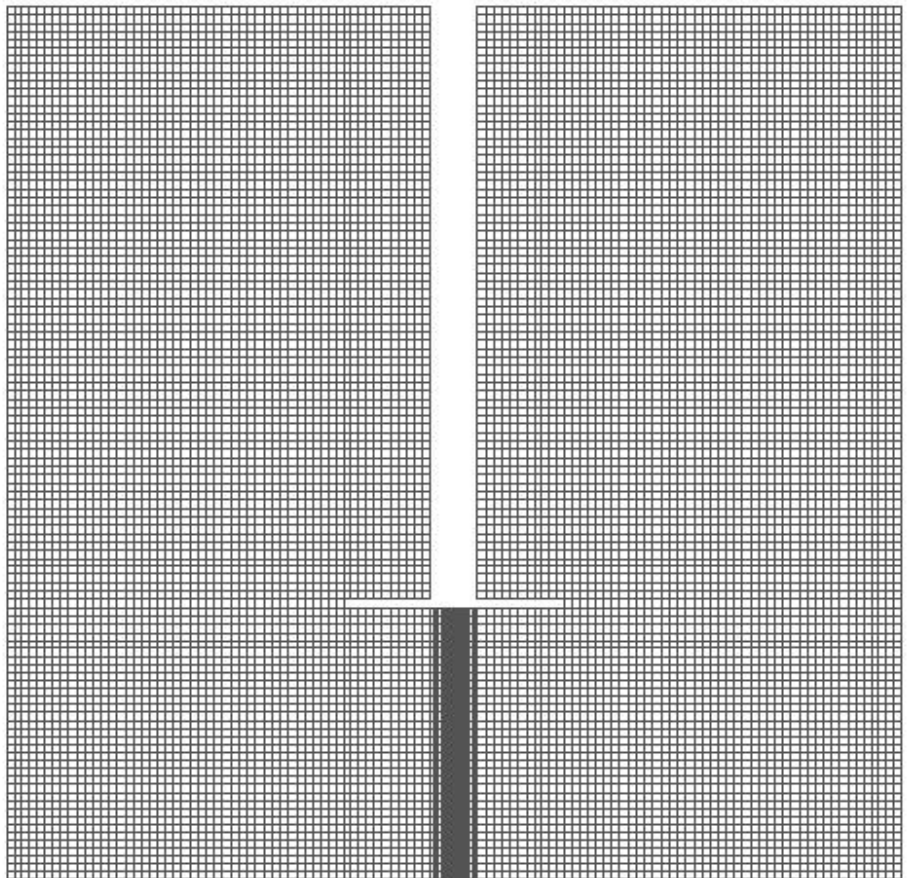

Figure 10 Grid of structured mesh, zero-thickness, side view (hexagonal, 670k)

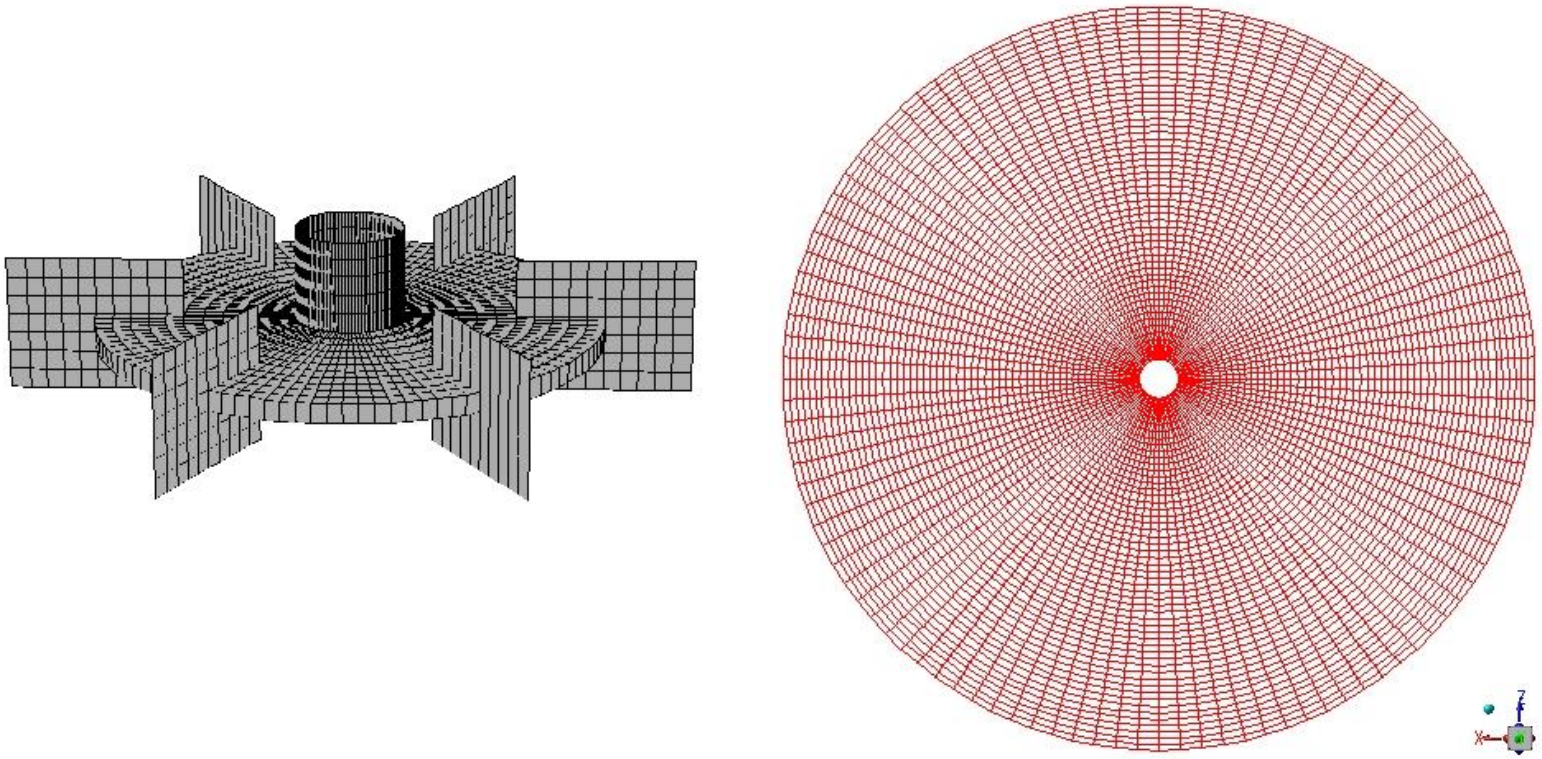

Figure 11 Grid of structured mesh, zero-thickness, rotor and top view (hexagonal, 670k)

4. Simulation Results and Discussion

4.1 Sensitivity Test

Sensitivity tests were conducted assuming a uniform bubble distribution of 3.5mm, and the volume-integrated turbulence dissipation rate (ϵ) and gas-holdup were adopted as criteria for mesh performance evaluation. In conclusion, the unstructured mesh and the structured mesh with zero-thickness models showed inferior performance compared to the normal structured mesh model. The unstructured mesh model was not able to reach convergence when QUICK scheme was used in the momentum equation. Even when QUICK scheme was mitigated to 1st order upwind scheme, the volume-integrated turbulence dissipation rate was predicted to be less than 30% compared to the structured mesh using QUICK scheme. On the other hand, zero-thickness mesh model also showed under predicted results compared to the structured mesh with thickness, with overall gas-holdup as 3.98% and $N_{P,diss}$ as 1.2. As shown in Figure 12, the zero-thickness mesh model predicts relatively fewer cavities behind the blades than the structured mesh with thickness. Therefore, the structured mesh was chosen as the appropriate mesh form for this work. Then, the additional sensitivity test for the refinement of the structured, thickness mesh was performed. There was no significant difference for more than 729k elements, hence a 729k mesh was used for subsequent simulations. The results for each mesh are summarized in Table 2.

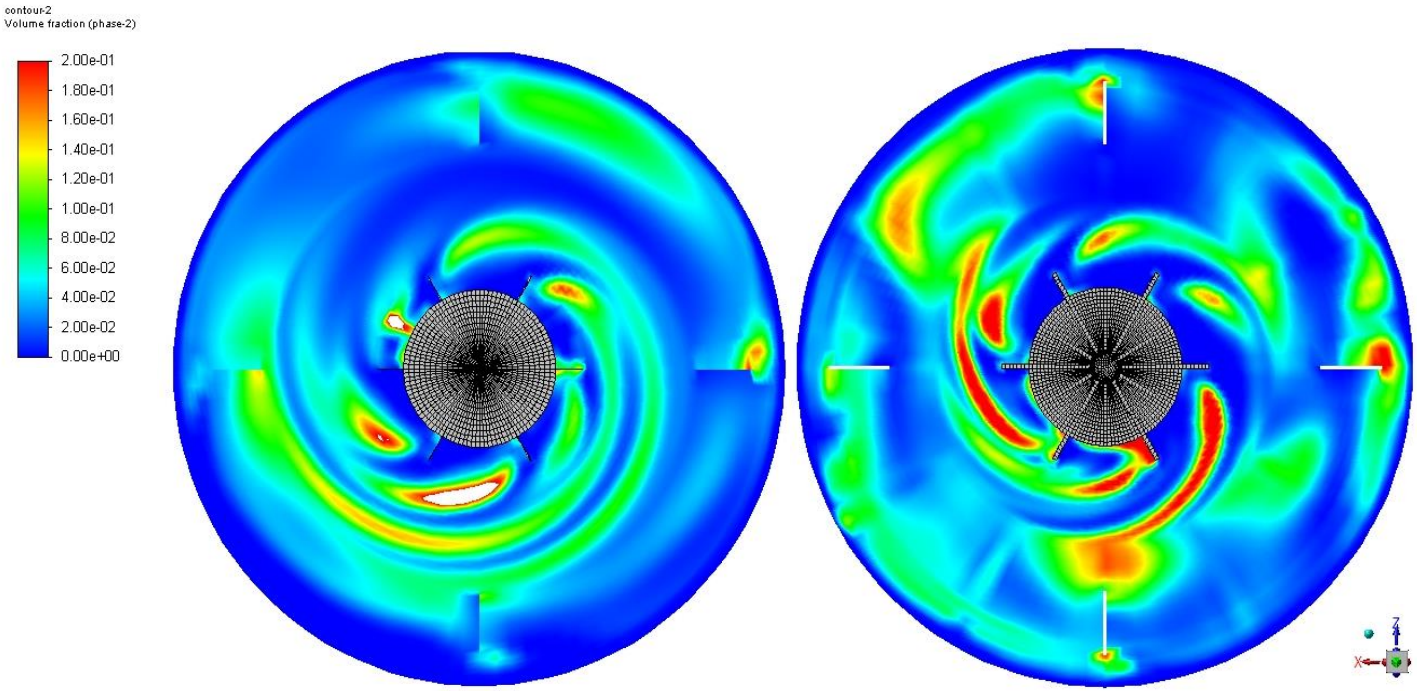

Figure 12 Contours of gas volume fraction around the impeller (Left: zero-thickness, Right: 4mm-thickness)

Table 2 Results of mesh sensitivitiy test

구분	elements #	momentum scheme	Overall gas-holdup[%]	Np,diss
hexa	419k	QUICK	4.44%	0.96
	666k	1st	5.39%	0.67
		QUICK	4.35%	1.55
	729k	QUICK	4.52%	1.66
	930k	QUICK	4.38%	1.70
Poly	288k	QUICK	Divergence	
	522k	QUICK	Divergence	
hexagonal, Zero-thickness	670k	QUICK	3.98%	1.20

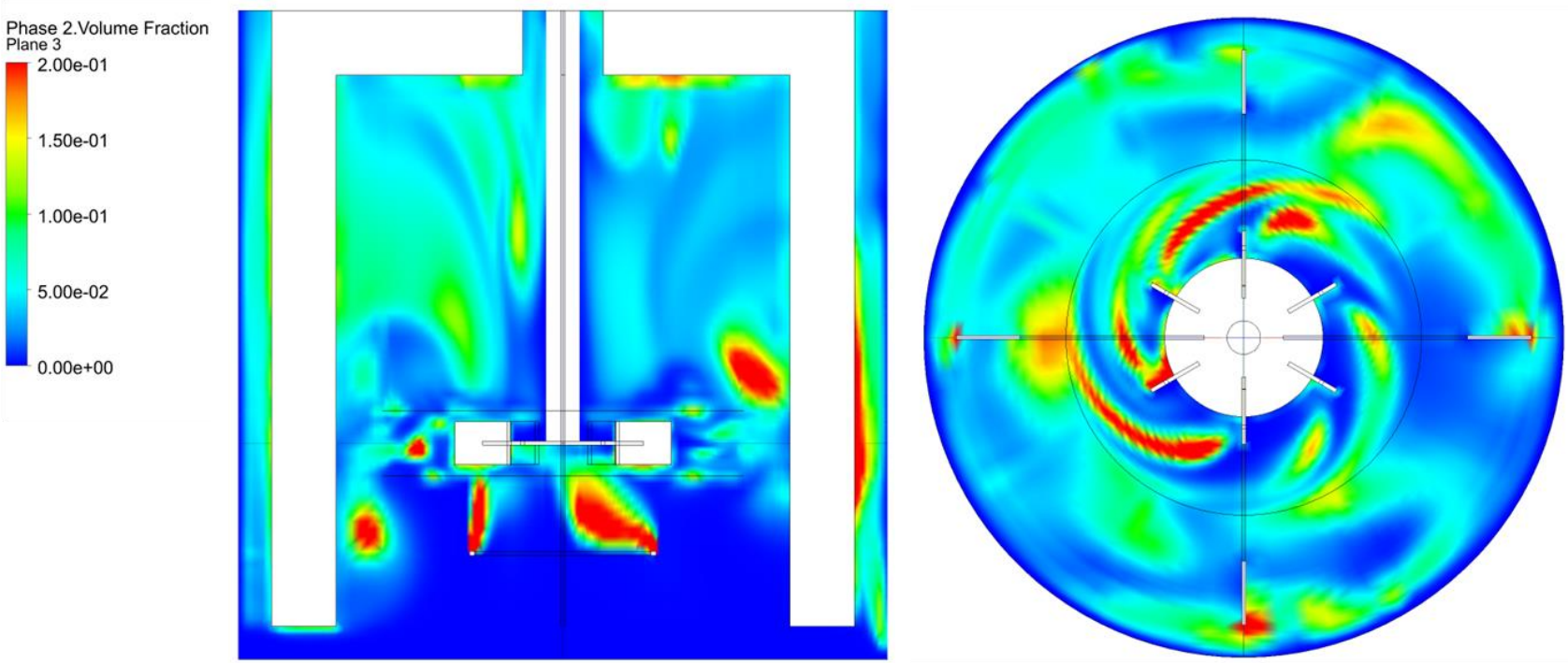

Figure 13 Contours of gas volume fraction (Left: side view, Right: impeller view)

4.2 Parameter Estimation

Parameter estimation of the coalescence and breakage kernel parameter C_1, C_3 (Eq. (36), (39)) was conducted. The root means square (RMS) error between local bubble size measurement and simulation bubble size results at 5 points (See Figure 4) was selected as the objective function. The EI was selected as the acquisition function. BO was performed on a sampling space discretized with 51 and 101 points for C_1 and C_3, respectively. The sampling range for each parameter is set to $0.5 \leq C_1 \leq 1.5$ and $3 \leq C_2 \leq 6$. It was considered that the theoretical value of C_1 is 0.88, and the range of C_3 values used in earlier studies ranged 2.52 to 6 [8, 24]. The sampling process was performed with the following sampling points recommended as a result of BO and intuition-based exploration grid search. After 10 sampling points were identified, the EI was lowered from the initial value 6.8e-2 to 4.93e-3, and the RMS error with the measurement was lowered from 2.73 to 0.7. This is a smaller error than existing research results [2, 8, 9]. The final values of parameters were determined to be 0.88 for C_1, and 5.6 for C_3, respectively. The changes in the sampling space's EI and the predicted objective function values as BO progresses are shown in Figure 14, Figure 15, Figure 16.

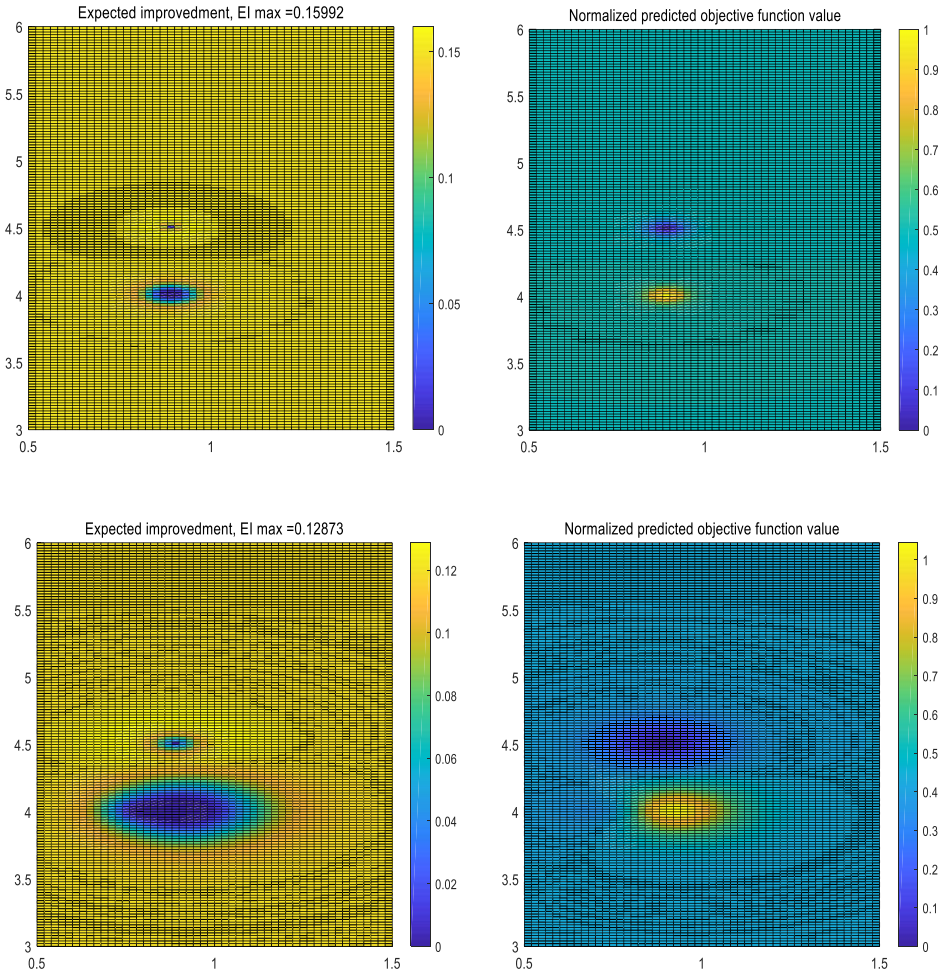

Figure 14 BO progress 1

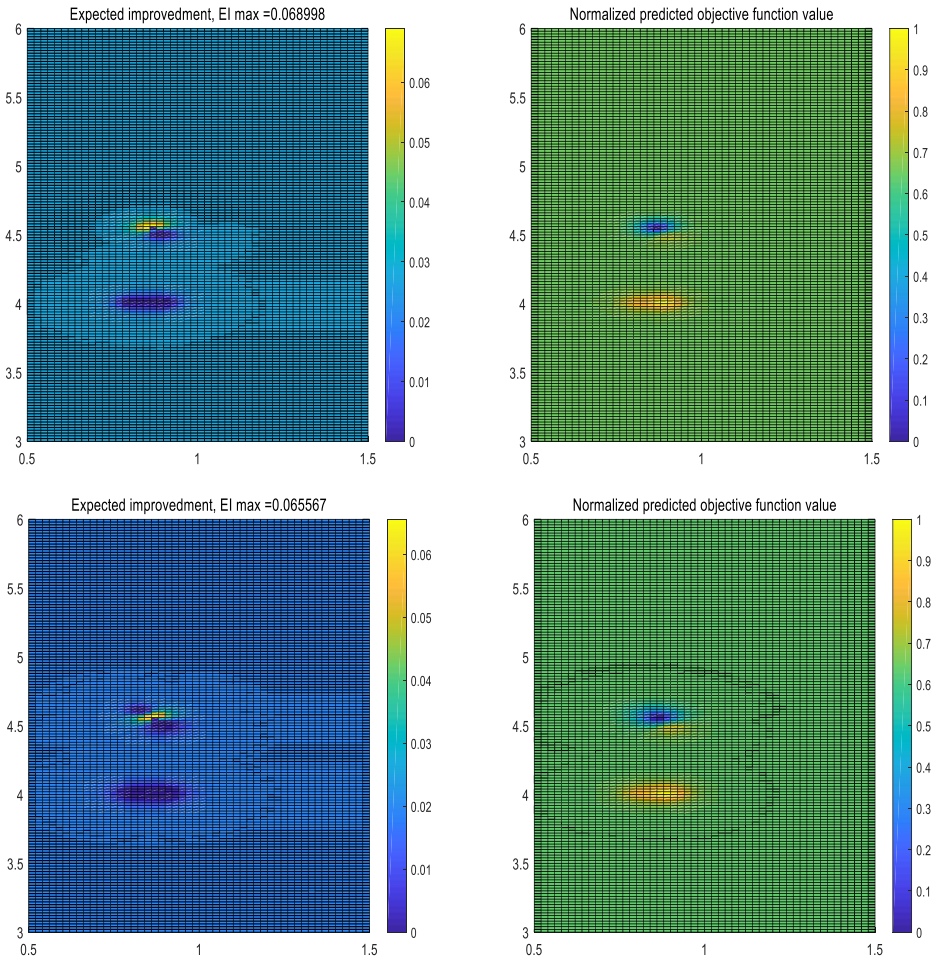

Figure 15 BO progress 2

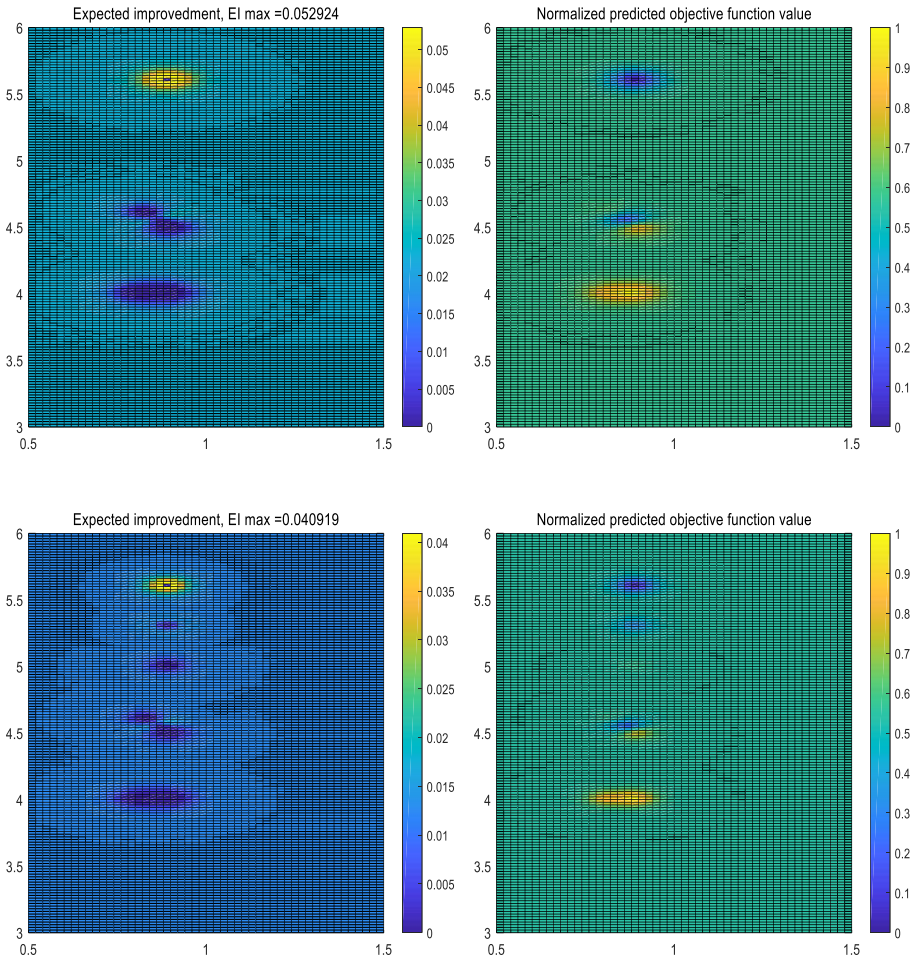

Figure 16 BO progress 3

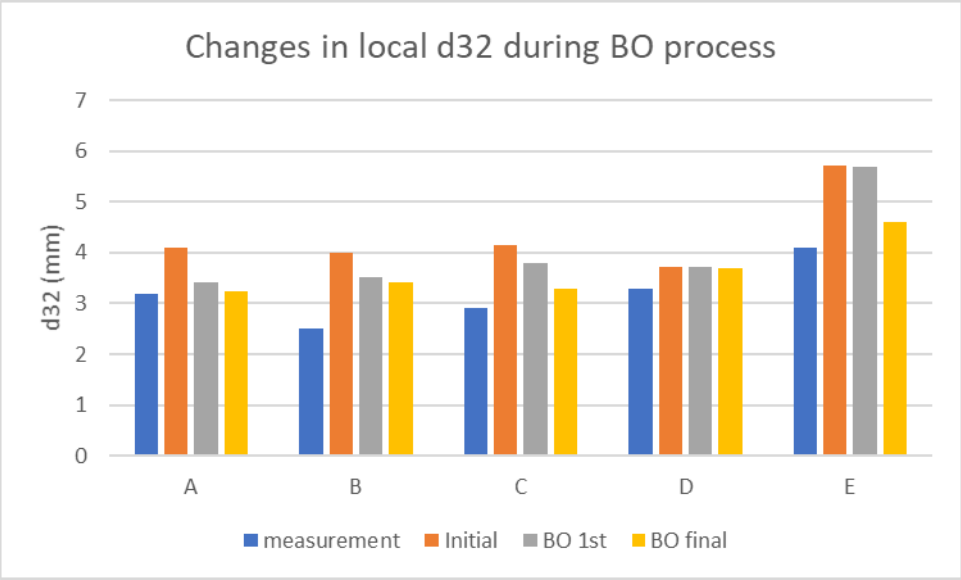

Figure 17 Changes in local d32 during BO process

4.3 Model Validation

The results of the final model with parameter estimation completed are as follows: Overall gas hold-up 4.35 %, $N_{p,diss}$ 1.60. The predicted overall gas holdup is in fairly good agreement with the experimental measurement value, 6% [8]. The power number (N_p) depends on the type of turbine, aeration rate, and even the blade thickness [61, 62]. In this work, the aeration rate is 0.7vvm and the ratio of blade thickness and turbine diameter of the Rushton turbine tank is 0.02. The N_p of this system is estimated as 2.2 [2]. However, it is well known that $N_{p,diss}$ can have an under-estimated value of N_p. According to Laakkonen, models shown good agreement with experimental data has $N_{p,diss}$ value around 1.2. Therefore, in this case, the $N_{p,diss}$ value of 1.6 is acceptable.

Local bubble size experimental measurement results and simulation results are compared. The RMS error of the model and measurement results is 0.7, which is improved over the results of the previous works using the same QMOM method [9]. The comparisons with prior studies are summarized in Figure 18.

The volume-averaged $K_L a$ is 0.0465, which shows good agreement with measurement results [8]. While the oxygen concentration equilibrium is typically achieved over 100s, the equilibrium of hydrodynamics reaches within 10s, therefore, the dynamics of the oxygen mass transfer rate is negligible. Under the assumption of a well-mixed liquid phase, the volume-averaged oxygen concentration, $C_o\ (t)$, can be evaluated as follows:

$$C_o(t) = C_o^*\left(1 - e^{-<k_L a>t}\right) - C_o(0)e^{-<k_L a>t} \tag{54}$$

where C_o^* is the oxygen solubility in water. Comparison of the volume-averaged oxygen concentration,

$C_o(t)$ in this model and prior studies was shown in ***Figure 21***.

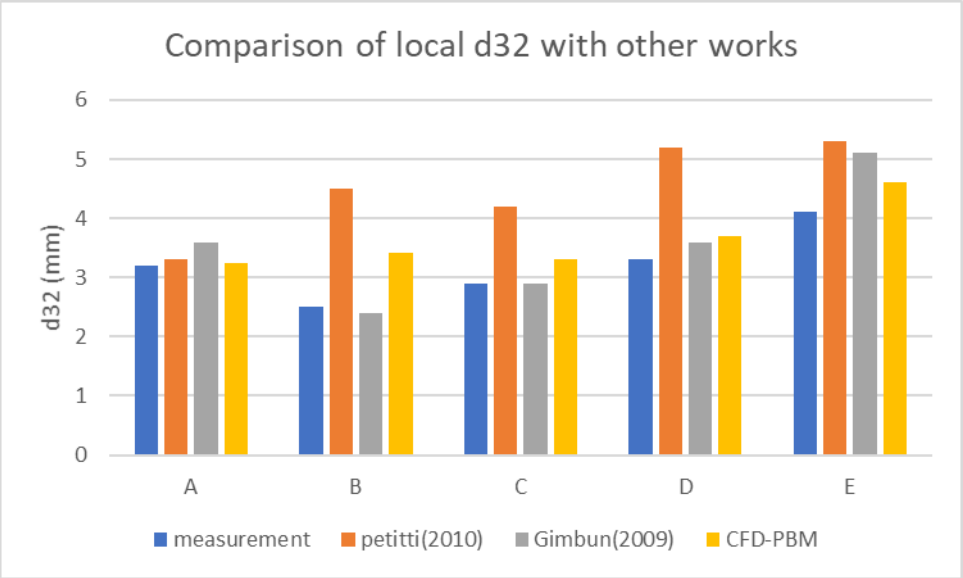

Figure 18 Comparison of local bubble Sauter mean (d32) with previous works and this work(CFD-PBM)

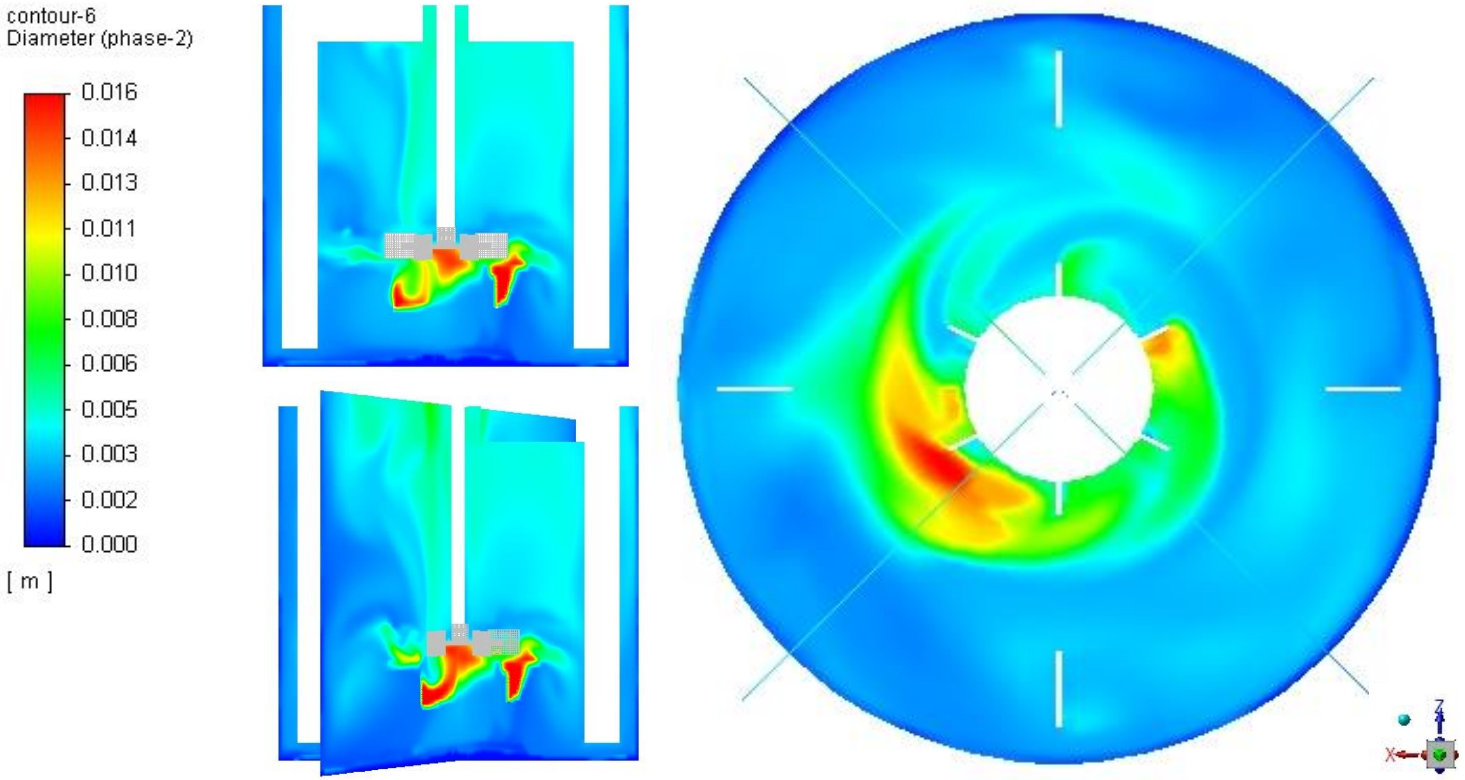

Figure 19 Contour of Bubble size (Left: side view, Right: Impeller view)

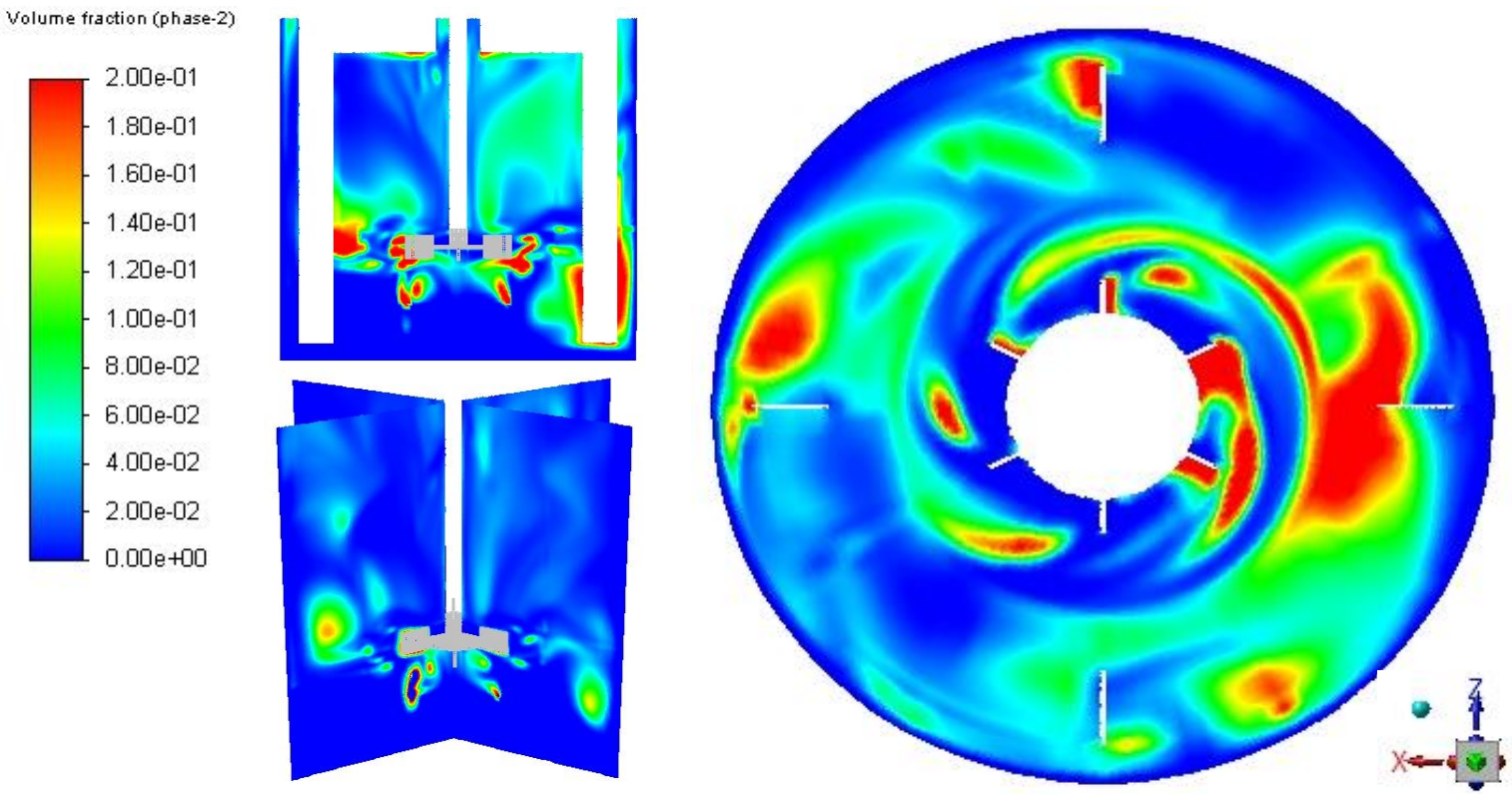

Figure 20 Contour of gas volume fraction (Left: side view, Right: Impeller view)

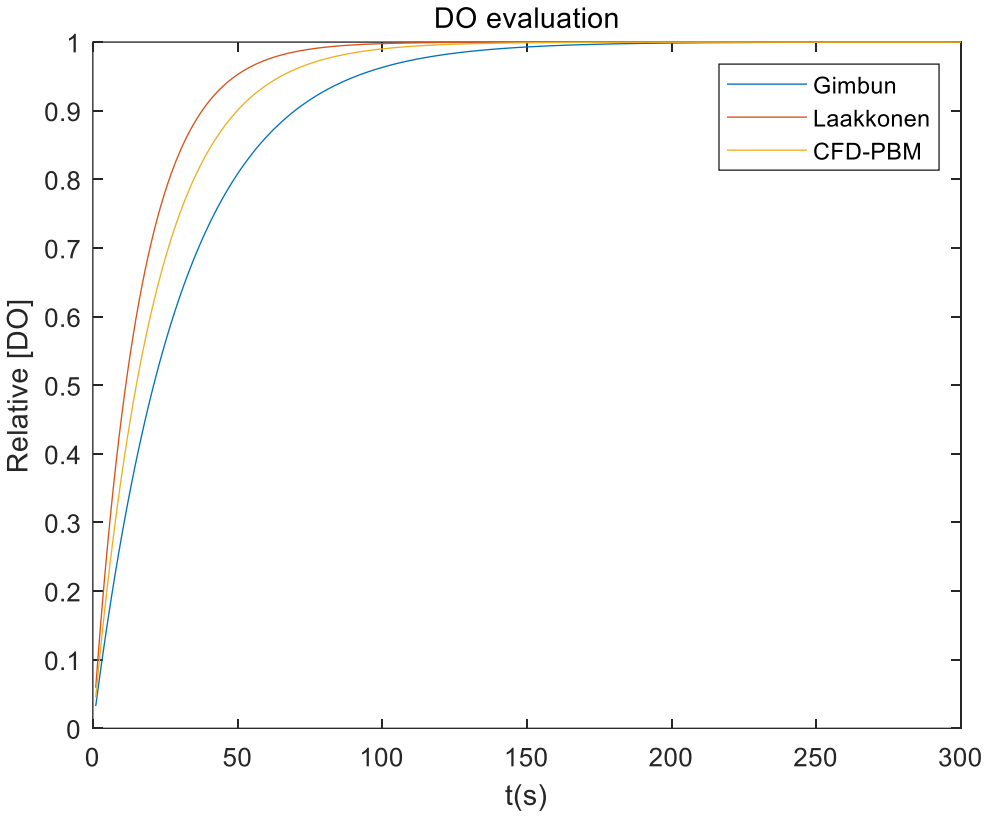

Figure 21 Comparison of evaluated DOs.

The Laakkonen model was fitted to the DO measurements data.

4.4 Comparison between Uniform Size Model and PBM Model

Comparison between the uniform, 3.5mm, bubble size model and PBM model was performed. Although the overall gas holdup was underestimated by the PBM model is closer to the volume-averaged oxygen transfer measurement. The overall gas holdup of the PBM model and the uniform bubble size model was 4.35% and 4.47% respectively, and the volume-averaged oxygen mass transfer were 0.0465 and 0.0455 s^{-1}. The reason for this difference is considered to be that the PBM model can reflect the effect of bubble size changing, such as local interfacial area.

The volume-averaged d32 of the PBM model was 3.22mm, similar to that of the uniform bubble size model. To analyze the difference between spatial distribution, the tank was divided into three regions: top, impeller, and bottom to compare the region-averaged d32 and $K_L a$. The analysis showed that the two models differed, especially in terms of predicting the occurrence of dead zones. The dead zone is defined as the place where the local oxygen mass transfer is lower than half of the volume-averaged $K_L a$, 0.025. The PBM model predicted that the dead zone was 37.93% of the reactor, while the uniform size model was 35.36%. In the bottom and top regions, the PBM models predicted 61.92% and 43.68% dead zones, and the uniform bubble size model predicted 65.25% and 40% dead zones, respectively. Consequently, since the larger volume fraction of dead zones could be predicted even at the larger volume-averaged oxygen mass transfer level, the PBM model better reflects the heterogeneity of the system.

In addition, the uniform bubble model is based on the estimation that the volume-averaged bubble size of the tank is 3.5mm. This is not only an estimated hypothesis based on the results of existing PBM researches but also an assumption that varies significantly depending on the target system. On the other

hand, the PBM model is based on the inlet bubble size distribution measured in the sparger, thus it is a more universal model that is not affected by the target system.

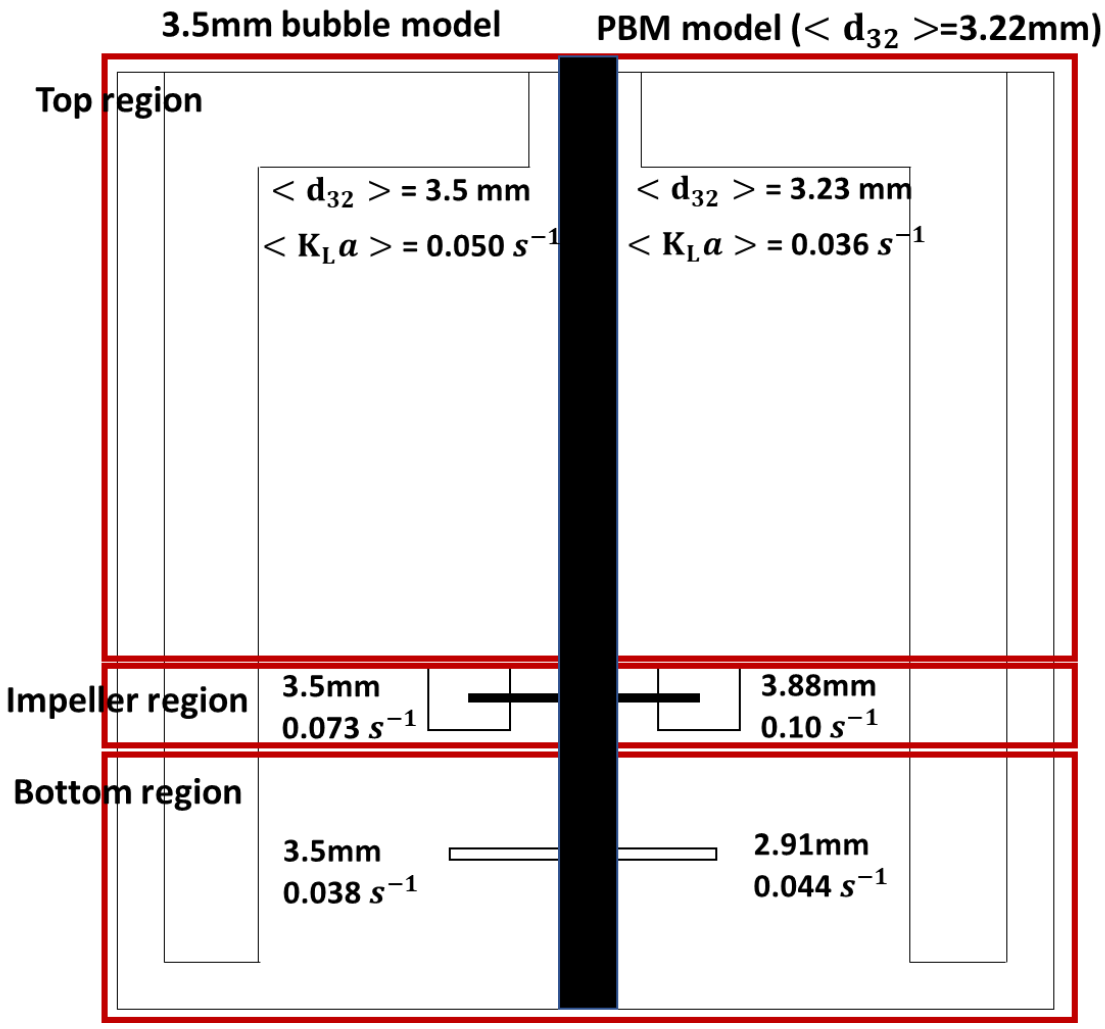

Figure 22 Comparison of region-averaged d32 and $K_L a$ results

(Left half: uniform bubble model, Right half: PBM model)

4.5 Oxygen Mass Transfer Rate Results in Viscosity Changes

The previous results of models and prior studies focused only on predicting a general water-air system with a viscosity of 1cp. However, according to Goldrick [23], the viscosity of the solution at the industrial scale bioreactor increases more than 10 times as the operation progresses, at an initial level of 1 cp. [48]. Furthermore, the empirical expressions of the volume-averaged oxygen mass transfer rate suggest that the volume-averaged oxygen mass transfer is inversely proportional to the 0.4 to 0.7 order of viscosity. In this work, based on the validated CFD-PBM model, a case study was conducted on how the oxygen mass transfer pattern changes according to the viscosity change.

The results were analyzed 7 different viscosity, 1, 2, 3, 4, 5, 7, 10 cp, and summarized in, Figure 24, Figure 25. As the viscosity increased, the mass transfer rate decreased. The mass transfer was inversely proportional to the 0.653 order of viscosity. These results are consistent with the existing empirical correlations. The dead zone increased from 40% to 90% of the entire reactor as the viscosity increased. $<K_L a>$ and <d32> were found to decrease in all regions. Additional analyzes were performed to determine how much reduced mass transfer was recovered with increasing mixing speed or aeration rate. At 3cp liquid, it was estimated that 67% and 45% of the mass transfer loss were recovered for an increase in mixing rate of 5% or an increase in aeration rate of 10%, respectively.

Viscosity [cp]		1	2	3	4	5	7	10
Gas hold-up [%]		4.35	4.41	4.31	4.11	3.56	3.24	3.21
d32 [mm]	Total	3.22	3.2	5	7.09	11.51	12.72	12.91
	Top	3.23	3.52	5.78	8.18	13.97	14.55	15.03
	Mid	3.88	3.34	5.23	6.78	8.25	9.53	9.49
	Bot	2.91	2.45	3.2	4.81	7.44	10.01	9.62
K_{la} [s^{-1}]	Total	0.0465	0.039	0.0284	0.0224	0.0156	0.0127	0.0129
	Top	0.0364	0.0278	0.0206	0.0167	0.0111	0.00905	0.00827
	Mid	0.103	0.0842	0.067	0.052	0.0488	0.0398	0.0426
	Bot	0.0444	0.0442	0.0289	0.0219	0.0121	0.0096	0.011

Figure 23 Case study summary

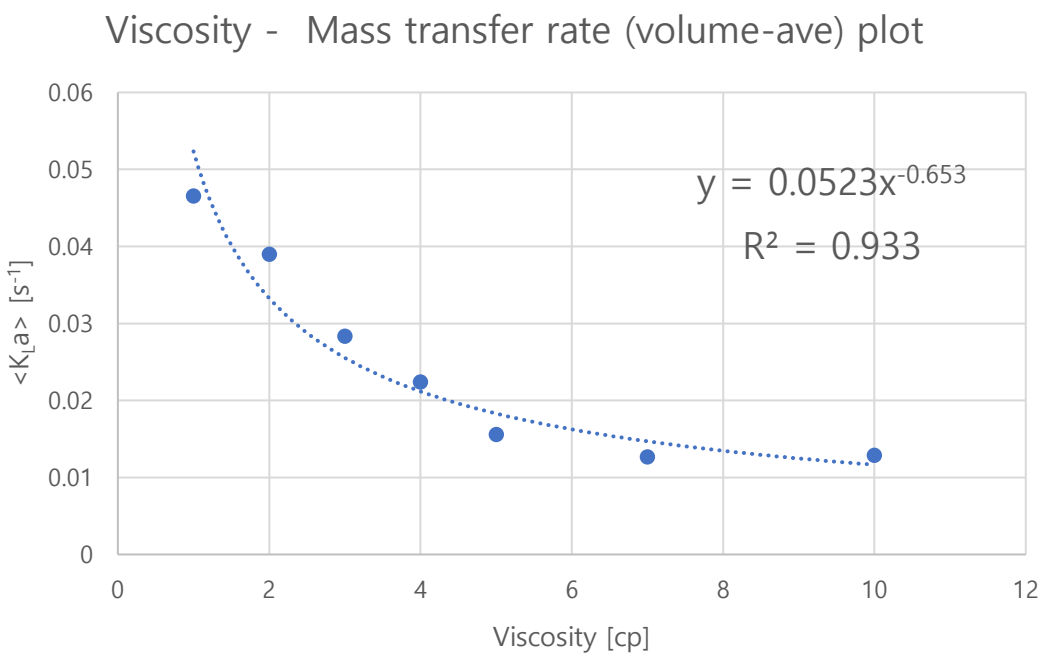

Figure 24 Change in volume-averaged mass transfer rate according to viscosity.

The mass transfer rate was inversely proportional to the -0.653 power of the viscosity, and the results are consistent with known empirical correlations.

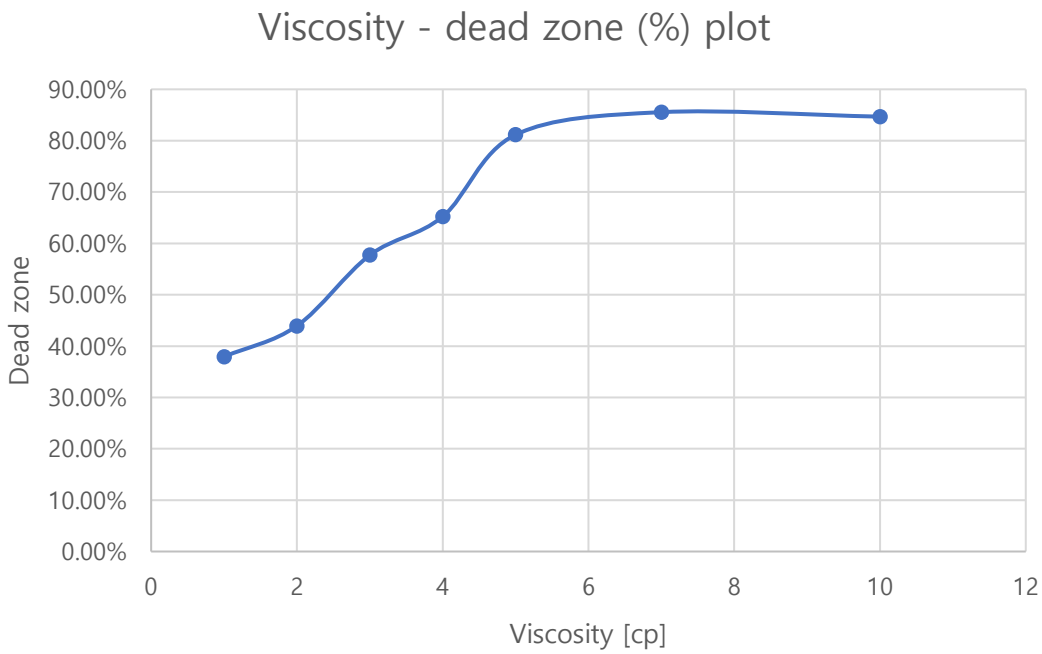

Figure 25 Change in dead-zone occurrence according to viscosity.

The dead-zone, which was 38% at 1 cp, increased to 85% at 10 cp.

5. Conclusion

A CFD-PBM coupled model that can reflect the heterogeneous hydrodynamics of the 200L baffled, stirred tank. Comparison and analysis of various mesh structures confirm that the results and stability of numerical methods are significantly influenced by mesh structure. The higher-order momentum discretization scheme, QUICK, was employed to simulate turbulence at a suitable level, and the mesh that can give stable results was also selected. During the mesh sensitivity test, it was found that the unstructured and zero-thickness structured meshes cannot provide sufficient performance, such as diverging or predicting severely under-estimated turbulent dissipation rate value.

Parameter estimation was carried out for accurate bubble dynamics simulation. Due to the non-linearity of the CFD-PBM model, a time-consuming grid search was inevitable. However, as a result of conducting an efficient design of experiments using Bayesian optimization, suitable parameters could be found even with about 10 searches. The final model showed better agreement than those reported in previous studies with 5 points of local bubble size measurement data, and the volume-averaged oxygen mass transfer rate also showed good agreement with the measurement. Compared with the uniform bubble size model, the PBM model predicts the heterogeneity of the system more strongly. Furthermore, PBM models have better generality since it only requires the bubble size distribution of the input while the uniform bubble size model requires the average bubble size of the system, which often unmeasurable.

Based on the validated model, a case study was conducted to predict the change in the volume-averaged oxygen mass transfer rate change with a change in viscosity. It was found that the volume-averaged oxygen mass transfer rate decreased by 28% as the viscosity increased 10 times, and an increase in the mixing rate of 5% and the aeration rate of 10% was estimated to recover 67% and 45% of reduced mass transfer rate, respectively.

References

[1] M. Shuler and F. Kargi, "How cells grow," *Bioprocess engineering basic concepts,* pp. 168-170, 2002.

[2] J. Gimbun, C. D. Rielly, and Z. K. Nagy, "Modelling of mass transfer in gas–liquid stirred tanks agitated by Rushton turbine and CD-6 impeller: A scale-up study," *Chemical Engineering Research and Design,* vol. 87, no. 4, pp. 437-451, 2009.

[3] F. Vardar and M. Lilly, "Effect of cycling dissolved oxygen concentrations on product formation in penicillin fermentations," *European Journal of Applied Microbiology and Biotechnology,* vol. 14, no. 4, pp. 203-211, 1982.

[4] J. T. Cornelissen, F. Taghipour, R. Escudié, N. Ellis, and J. R. Grace, "CFD modelling of a liquid–solid fluidized bed," *Chemical Engineering Science,* vol. 62, no. 22, pp. 6334-6348, 2007.

[5] N. Qi, H. Zhang, K. Zhang, G. Xu, and Y. Yang, "CFD simulation of particle suspension in a stirred tank," *Particuology,* vol. 11, no. 3, pp. 317-326, 2013.

[6] M. V. Tabib, S. A. Roy, and J. B. Joshi, "CFD simulation of bubble column—an analysis of interphase forces and turbulence models," *Chemical Engineering Journal,* vol. 139, no. 3, pp. 589-614, 2008.

[7] F. Scargiali, A. D'Orazio, F. Grisafi, and A. Brucato, "Modelling and simulation of gas–liquid hydrodynamics in mechanically stirred tanks," *Chemical Engineering Research and Design,* vol. 85, no. 5, pp. 637-646, 2007.

[8] M. Laakkonen, P. Moilanen, V. Alopaeus, and J. Aittamaa, "Modelling local bubble size distributions in agitated vessels," *Chemical Engineering Science,* vol. 62, no. 3, pp. 721-740, 2007.

[9] M. Petitti *et al.*, "Bubble size distribution modeling in stirred gas–liquid reactors with QMOM augmented by a new correction algorithm," *AIChE Journal,* vol. 56, no. 1, pp. 36-53, 2010.

[10] G. Lane, M. Schwarz, and G. Evans, "Predicting gas–liquid flow in a mechanically stirred tank," *Applied Mathematical Modelling,* vol. 26, no. 2, pp. 223-235, 2002.

[11] P. Moilanen, M. Laakkonen, O. Visuri, V. Alopaeus, and J. Aittamaa, "Modelling mass transfer in an aerated 0.2 m3 vessel agitated by Rushton, Phasejet and Combijet impellers," *Chemical Engineering Journal,* vol. 142, no. 1, pp. 95-108, 2008.

[12] M. Laakkonen, M. Honkanen, P. Saarenrinne, and J. Aittamaa, "Local bubble size distributions, gas–liquid interfacial areas and gas holdups in a stirred vessel with particle image velocimetry," *Chemical Engineering Journal,* vol. 109, no. 1-3, pp. 37-47, 2005.

[13] G. Montante, D. Horn, and A. Paglianti, "Gas–liquid flow and bubble size distribution in stirred tanks," *Chemical engineering science,* vol. 63, no. 8, pp. 2107-2118, 2008.

[14] T. Wang, J. Wang, and Y. Jin, "Population balance model for gas− liquid flows: Influence of bubble coalescence and breakup models," *Industrial & Engineering Chemistry Research,* vol. 44, no. 19, pp. 7540-7549, 2005.

[15] M. Sen and R. Ramachandran, "A multi-dimensional population balance model approach to continuous powder mixing processes," *Advanced Powder Technology,* vol. 24, no. 1, pp. 51-59, 2013.

[16] Z. Chen, J. Prüss, and H.-J. Warnecke, "A population balance model for disperse systems: drop size distribution in emulsion," *Chemical Engineering Science,* vol. 53, no. 5, pp. 1059-1066, 1998.

[17] R. Dürr and A. Bück, "Approximate Moment Methods for Population Balance Equations in Particulate and Bioengineering Processes," *Processes,* vol. 8, no. 4, p. 414, 2020.

[18] R. Maltby, S. Tian, and Y. J. Chew, "Computational studies of a novel magnetically driven single-use-technology bioreactor: A comparison of mass transfer models," *Chemical Engineering Science,* vol. 187, pp. 157-173, 2018.

[19] R. McGraw, "Description of aerosol dynamics by the quadrature method of moments," *Aerosol Science and Technology,* vol. 27, no. 2, pp. 255-265, 1997.

[20] S. Mishra, V. Kumar, J. Sarkar, and A. S. Rathore, "CFD based mass transfer modeling of a single use bioreactor for production of monoclonal antibody biotherapeutics," *Chemical Engineering Journal,* vol. 412, p. 128592, 2021.

[21] F. García-Ochoa and E. Gómez, "Mass transfer coefficient in stirred tank reactors for xanthan gum solutions," *Biochemical Engineering Journal,* vol. 1, no. 1, pp. 1-10, 1998.

[22] P. M. Kilonzo and A. Margaritis, "The effects of non-Newtonian fermentation broth viscosity and small bubble segregation on oxygen mass transfer in gas-lift bioreactors: a critical review," *Biochemical Engineering Journal,* vol. 17, no. 1, pp. 27-40, 2004.

[23] S. Goldrick, A. Ştefan, D. Lovett, G. Montague, and B. Lennox, "The development of an industrial-scale fed-batch fermentation simulation," *Journal of biotechnology,* vol. 193, pp. 70-82, 2015.

[24] A. Buffo, M. Vanni, and D. Marchisio, "Multidimensional population balance model for the simulation of turbulent gas–liquid systems in stirred tank reactors," *Chemical Engineering Science,* vol. 70, pp. 31-44, 2012.

[25] W. L. Haberman and R. K. Morton, "An experimental study of bubbles moving in liquids," *Transactions of the American Society of Civil Engineers,* vol. 121, no. 1, pp. 227-250, 1956.

[26] M. Ishii and N. Zuber, "Drag coefficient and relative velocity in bubbly, droplet or particulate flows," *AIChE journal,* vol. 25, no. 5, pp. 843-855, 1979.

[27] A. Tomiyama, I. Kataoka, I. Zun, and T. Sakaguchi, "Drag coefficients of single bubbles under normal and micro gravity conditions," *JSME International Journal Series B Fluids and Thermal Engineering,* vol. 41, no. 2, pp. 472-479, 1998.

[28] A. Behzadi, R. Issa, and H. Rusche, "Modelling of dispersed bubble and droplet flow at high phase fractions," *Chemical Engineering Science,* vol. 59, no. 4, pp. 759-770, 2004.

[29] D. L. Marchisio and R. O. Fox, *Computational models for polydisperse particulate and multiphase systems*. Cambridge University Press, 2013.

[30] L. Gemello, C. Plais, F. Augier, and D. L. Marchisio, "Population balance modelling of bubble columns under the heterogeneous flow regime," *Chemical Engineering Journal,* vol. 372, pp. 590-604, 2019.

[31] A. Randolph, *Theory of particulate processes: analysis and techniques of continuous crystallization*. Elsevier, 2012.

[32] D. L. Marchisio, R. D. Vigil, and R. O. Fox, "Quadrature method of moments for aggregation–breakage processes," *Journal of Colloid and Interface Science,* vol. 258, no. 2, pp. 322-334, 2003.

[33] H. Dette and W. J. Studden, *The theory of canonical moments with applications in statistics, probability, and analysis*. John Wiley & Sons, 1997.

[34] N. Lebaz, A. Cockx, M. Sperandio, and J. Morchain, "Reconstruction of a distribution from a finite number of its moments: a comparative study in the case of depolymerization process," *Computers & Chemical Engineering,* vol. 84, pp. 326-337, 2016.

[35] R. G. Gordon, "Error bounds in equilibrium statistical mechanics," *Journal of Mathematical Physics,* vol. 9, no. 5, pp. 655-663, 1968.

[36] J. C. Wheeler, "Modified moments and Gaussian quadratures," *The Rocky Mountain Journal of Mathematics,* vol. 4, no. 2, pp. 287-296, 1974.

[37] M. J. Prince and H. W. Blanch, "Bubble coalescence and break-up in air-sparged bubble columns," *AIChE journal,* vol. 36, no. 10, pp. 1485-1499, 1990.

[38] C. Coulaloglou and L. L. Tavlarides, "Description of interaction processes in agitated liquid-liquid dispersions," *Chemical Engineering Science,* vol. 32, no. 11, pp. 1289-1297, 1977.

[39] R. Shinnar and J. M. Church, "Statistical theories of turbulence in predicting particle size in agitated dispersions," *Industrial & Engineering Chemistry,* vol. 52, no. 3, pp. 253-256, 1960.

[40] W. Howarth, "Coalescence of drops in a turbulent flow field," *Chemical Engineering Science,* vol. 19, no. 1, pp. 33-38, 1964.

[41] F. Lehr, M. Millies, and D. Mewes, "Bubble-size distributions and flow fields in bubble columns," *AIChE Journal,* vol. 48, no. 11, pp. 2426-2443, 2002.

[42] Y. Liao and D. Lucas, "A literature review of theoretical models for drop and bubble breakup in turbulent dispersions," *Chemical Engineering Science,* vol. 64, no. 15, pp. 3389-3406, 2009.

[43] A. Aliseda, A. Cartellier, F. Hainaux, and J. C. Lasheras, "Effect of preferential concentration on the settling velocity of heavy particles in homogeneous isotropic turbulence," *Journal of Fluid Mechanics,* vol. 468, p. 77, 2002.

[44] V. Alopaeus, J. Koskinen, K. I. Keskinen, and J. Majander, "Simulation of the population balances for liquid–liquid systems in a nonideal stirred tank. Part 2—parameter fitting and the use of the multiblock model for dense dispersions," *Chemical Engineering Science,* vol. 57, no. 10, pp. 1815-1825, 2002.

[45] M. Laakkonen, V. Alopaeus, and J. Aittamaa, "Validation of bubble breakage, coalescence and mass transfer models for gas–liquid dispersion in agitated vessel," *Chemical Engineering Science,* vol. 61, no. 1, pp. 218-228, 2006.

[46] K. Van't Riet, "Review of measuring methods and results in nonviscous gas-liquid mass transfer in stirred vessels," *Industrial & Engineering Chemistry Process Design and Development,* vol. 18, no. 3, pp. 357-364, 1979.

[47] H. Yagi and F. Yoshida, "Gas absorption by Newtonian and non-Newtonian fluids in sparged agitated vessels," *Industrial & Engineering Chemistry Process Design and Development,* vol. 14, no. 4, pp. 488-493, 1975.

[48] F. Garcia-Ochoa and E. Gomez, "Bioreactor scale-up and oxygen transfer rate in microbial processes: an overview," *Biotechnology Advances,* vol. 27, no. 2, pp. 153-176, 2009.

[49] R. Wellek, A. Agrawal, and A. Skelland, "Shape of liquid drops moving in liquid media," *AIChE Journal,* vol. 12, no. 5, pp. 854-862, 1966.

[50] S. Guet, S. Luther, and G. Ooms, "Bubble shape and orientation determination with a four-point optical

fibre probe," *Experimental Thermal and Fluid Science,* vol. 29, no. 7, pp. 803-812, 2005.

[51] R. Higbie, "The rate of absorption of a pure gas into a still liquid during short periods of exposure," *Trans. AIChE,* vol. 31, pp. 365-389, 1935.

[52] J. C. Lamont and D. Scott, "An eddy cell model of mass transfer into the surface of a turbulent liquid," *AIChE Journal,* vol. 16, no. 4, pp. 513-519, 1970.

[53] S. Park, J. Na, M. Kim, and J. M. Lee, "Multi-objective Bayesian optimization of chemical reactor design using computational fluid dynamics," *Computers & Chemical Engineering,* vol. 119, pp. 25-37, 2018.

[54] J. Mockus, *Bayesian approach to global optimization: theory and applications*. Springer Science & Business Media, 2012.

[55] D. R. Jones, M. Schonlau, and W. J. Welch, "Efficient global optimization of expensive black-box functions," *Journal of Global Optimization,* vol. 13, no. 4, pp. 455-492, 1998.

[56] J. Derksen, M. Doelman, and H. Van den Akker, "Three-dimensional LDA measurements in the impeller region of a turbulently stirred tank," *Experiments in Fluids,* vol. 27, no. 6, pp. 522-532, 1999.

[57] M. Coroneo, G. Montante, A. Paglianti, and F. Magelli, "CFD prediction of fluid flow and mixing in stirred tanks: Numerical issues about the RANS simulations," *Computers & Chemical Engineering,* vol. 35, no. 10, pp. 1959-1968, 2011.

[58] W. Bujalski, A. Nienow, S. Chatwin, and M. Cooke, "The dependency on scale of power numbers of Rushton disc turbines," *Chemical Engineering Science,* vol. 42, no. 2, pp. 317-326, 1987.

[59] K. Rutherford, S. Mahmoudi, K. Lee, and M. Yianneskis, "The influence of Rushton impeller blade and disk thickness on the mixing characteristics of stirred vessels," *Chemical Engineering Research & Design,* vol. 74, no. 3, pp. 369-378, 1996.

[60] R. Zadghaffari, J. Moghaddas, and J. Revstedt, "A mixing study in a double-Rushton stirred tank," *Computers & Chemical Engineering,* vol. 33, no. 7, pp. 1240-1246, 2009.

[61] D. Chapple, S. Kresta, A. Wall, and A. Afacan, "The effect of impeller and tank geometry on power number for a pitched blade turbine," *Chemical Engineering Research and Design,* vol. 80, no. 4, pp. 364-372, 2002.

[62] J. Smith, "Large multiphase reactors: some open questions," *Chemical Engineering Research and Design,* vol. 84, no. 4, pp. 265-271, 2006.

Abstract in Korean (국문 초록)

본 석사학위 논문에서는 기-액 교반 탱크의 산소 물질 전달 속도 예측을 위한 CFD-PBM 통합 모델을 제시한다. 안정적인 수치 해석을 위해 세 가지 메쉬 (비 정형, 두께를 고려한 정형, 두께를 생략한 정형 메쉬)가 비교, 분석되었고, 두께를 고려한 정형 메쉬가 최종적으로 선택되었다. 이후 PBM kernel들의 조정 가능한 파라미터들이 추정되었다. CFD-PBM 모델의 강한 비 선형성 때문에 격자 탐색이 활용되었으며, 최대한 효율적인 격자 탐색을 위해 베이지안 최적화 (BO)가 활용되었다. 최종 모델이 실험 측정 결과로 검증되었고, 검증된 모델과 단일 크기 거품 모델의 결과가 비교되었다. 비교 결과, PBM 모델은 시스템의 비균질성을 더 잘 반영하며, 그래서 교반 탱크에서 'dead zone'의 발생을 더 잘 예측하는 것으로 나타났다. 마지막으로, 점도 변화에 따른 산소 물질전달량 변화 양상을 파악하기 위한 연구가 진행되었다. 결과적으로, 물의 점도가 열 배로 증가함에 따라 산소 물질전달량은 72% 만큼 감소하며, 3 배 수준의 점도에서 혼합 속도를 약 5% 정도 증가시키거나 공기 주입량을 10% 증가시키면 각각 감소한 물질전달량의 67% 와 45%를 회복하는 것으로 추정되었다.

주요어: 전산 유체 역학, 다상유동, 입자 개체군 수지식, 산소 물질 전달량, 생물 반응기, 점도

학번: 2019-29645